

# *XMM-Newton* observations of the Galactic Supernova Remnant CTB 109 (G109.1–1.0)

Manami Sasaki  
msasaki@cfa.harvard.edu

Paul P. Plucinsky

Terrance J. Gaetz

Randall K. Smith

Richard J. Edgar  
and

Patrick O. Slane  
*Harvard-Smithsonian Center for Astrophysics, 60 Garden Street, Cambridge, MA 02138*

## ABSTRACT

We present the analysis of the X-ray Multi-Mirror Mission (*XMM-Newton*) European Photon Imaging Camera (EPIC) data of the Galactic supernova remnant (SNR) CTB 109 (G109.1–1.0). CTB 109 is associated with the anomalous X-ray pulsar (AXP) 1E 2259+586 and has an unusual semi-circular morphology in both the X-ray and the radio, and an extended X-ray bright interior region known as the ‘Lobe’. The deep EPIC mosaic image of the remnant shows no emission towards the west where a giant molecular cloud complex is located. No morphological connection between the Lobe and the AXP is found. We find remarkably little spectral variation across the remnant given the large intensity variations. All spectra of the shell and the Lobe are well fitted by a single-temperature non-equilibrium ionization model for a collisional plasma with solar abundances ( $kT \approx 0.5 - 0.7$  keV,  $\tau = \int n_e dt \approx 1 - 4 \times 10^{11}$  s cm $^{-3}$ ,  $N_H \approx 5 - 7 \times 10^{21}$  cm $^{-2}$ ). There is no indication of nonthermal emission in the Lobe or the shell. We conclude that the Lobe originated from an interaction of the SNR shock wave with an interstellar cloud. Applying the Sedov solution for the undisturbed eastern part of the SNR, and assuming full equilibration between the electrons and ions behind the shock front, the SNR shock velocity is derived as  $v_s = 720 \pm 60$  km s $^{-1}$ , the remnant age as  $t = (8.8 \pm 0.9) \times 10^3 d_3$  yr, the initial energy as  $E_0 = (7.4 \pm 2.9) \times 10^{50} d_3^{2.5}$  ergs, and the pre-shock density of the nuclei in the ambient medium as  $n_0 = (0.16 \pm 0.02) d_3^{-0.5}$  cm $^{-3}$ , at an assumed distance of  $D = 3.0 d_3$  kpc. Assuming CTB 109 and 1E 2259+586 are associated, these values constrain the age and the environment of the progenitor of the SNR and the pulsar.

*Subject headings:* shock waves — supernova remnants — X-rays: individual (CTB 109) — ISM: individual (CTB 109)

## 1. Introduction

The Galactic supernova remnant (SNR) CTB 109 (G109.2-1.0) was discovered in X-rays with *Einstein* by Gregory & Fahlman (1980). In the radio band, it was identified as an SNR by Hughes et al. (1981) in the Galactic plane survey at  $\lambda 49$  cm with the Westerbork Synthesis Radio Telescope. CTB 109 is the host remnant of the anomalous X-ray pulsar (AXP) 1E2259+586 with a spin period of  $P = 6.98$  s (Fahlman & Gregory 1981, 1983) and a spin-down rate of  $3 - 6 \times 10^{-13}$  s s $^{-1}$  (Iwasawa et al. 1992). In 2002, an outburst of 1E2259+586 occurred with bursts similar to Soft Gamma Repeaters and with a sudden spin up of  $\delta\nu/\nu = 4 \times 10^{-6}$  (Kaspi et al. 2003; Gavriil et al. 2003; Woods et al. 2004).

The distance to the SNR has been estimated from various observations as 3 – 6 kpc (Sofue et al. 1983; Hughes et al. 1984; Kothes et al. 2002, and references therein). A distance of  $3.0 \pm 0.5$  kpc has been derived by Kothes et al. (2002) by measuring the spectroscopic distances and radial velocities of H II regions and comparing those values to the radial velocity of CTB 109 measured by Tatematsu et al. (1990). The remnant is embedded in a large complex of H II regions which extends over 400 pc along the Galactic plane.

At radio frequencies, Hughes et al. (1984) have derived a spectral index of  $\alpha = 0.50 \pm 0.04$ , for flux density  $S_\nu \propto \nu^{-\alpha}$  and frequency  $\nu$ , which does not vary across the remnant. The remnant shell is incomplete in the west, both in radio and X-rays (see Fig. 1). Bright spots are found around the rim, but the features do not correlate in the two bands. No radio point source is found at the position of the X-ray pulsar, which is displaced by  $3'6$  from the geometrical center of the radio shell.

CTB 109 is located near a giant molecular cloud (GMC) complex (Israel 1980) which contains five H II regions. Heydari-Malayeri et al. (1981) and Tatematsu et al. (1985) have suggested that this GMC complex is associated with the SNR based on CO and  $^{13}\text{CO}$  observations. Data from the Position Sensitive Proportional Counter (PSPC) of the Röntgensatellit (*ROSAT*) confirm that there is no X-ray emission in the west (Rho & Petre 1997, hereafter RP97). The SNR shell does not extend further to the west behind the GMC in either radio or X-rays; because absorption is neg-

ligible in the radio continuum, this implies that the semi-circular shape of the remnant is not due to absorption. More likely, the SNR shock has been stopped by the GMC complex on one side. To the east, the interstellar medium (ISM) density appears to be lower, as indicated in the H I map of Kothes et al. (2002). In CO ( $J = 1 - 0$ ) and  $^{13}\text{CO}$  ( $J = 1 - 0$ ) observations, Tatematsu et al. (1987) have found an arm-like CO ridge ('CO arm') which is anti-correlated with the X-ray emission.

CTB 109 has a strikingly bright region in X-rays in the interior, the 'X-ray blob' or the 'Lobe'. Gregory & Fahlman (1983) have suggested that the AXP emits a jet and that the bright Lobe is material excited by a jet or the jet itself. However, Rho & Petre (1993, 1997) have shown that the *ROSAT* PSPC spectrum of the Lobe is thermal in origin and shows no evidence of synchrotron emission, arguing against a jet interpretation. Hurford & Fesen (1995) have found no morphological evidence to support a pulsar jet origin for the Lobe in the *ROSAT* High Resolution Imager (HRI) data and conclude that the bright X-ray emission from the Lobe is most likely caused by a density enhancement in material stripped from the cloud complex. Finally, the *Chandra* image (Patel et al. 2001) reveals no morphological connection between the Lobe and the AXP. Rho & Petre (1997) show that for parts of the shell, the X-ray spectrum is well fitted by a single-component thermal model, whereas for the Lobe and the northern and the southern part of the shell, two thermal components are required. A *BeppoSAX* Low-Energy Concentrator Spectrometer (LECS) spectrum of the whole SNR excluding the pulsar and the Lobe has been analyzed by Parmar et al. (1998). The parameters of the best fit to the LECS data with a non-equilibrium model are  $kT = 0.95_{-0.27}^{+0.65}$  keV and the ionization timescale  $n_e t = 3.8_{-1.6}^{+3.8} \times 10^{11}$  cm $^{-3}$  s.

Surveys of Galactic SNRs have been performed with the Infrared Astronomical Satellite (*IRAS*), revealing infrared emission from CTB 109 (Arendt 1989; Saken et al. 1992). The data in the wavelength bands of 12, 25, 60, and 100  $\mu\text{m}$  show a dense dust cloud which is correlated with bright H II regions, located in the south and west of the remnant (Coe et al. 1989). Furthermore, an enhancement in infrared emission is found between the Lobe and the north-east shell.

Optical emission is detected mainly near the bright northeastern and southern radio emission (Hughes et al. 1981). Spectra of filamentary structures in the south confirm their shock origin (Blair & Kirshner 1981).  $H\alpha$  and  $[O\ III]$  images of Fesen & Hurford (1995) reveal previously unknown filaments, e.g. faint filaments near the projected center of the remnant, along the southwestern edge of the bright Lobe. From the filament spectra, they derive a shock velocity of  $\sim 100\text{ km s}^{-1}$  and pre-shock cloud densities of  $5 - 20\text{ cm}^{-3}$ .

We have undertaken observations of CTB 109 with the *XMM-Newton* observatory to provide the deepest X-ray image of this SNR and to provide the highest quality X-ray spectral data to date. The primary objectives of our analysis are to determine the evolutionary parameters of the remnant assuming it is in the Sedov phase and to determine the nature of the Lobe emission. The deep X-ray images are used to study the morphology of this remnant in comparison to the data at other wavelengths and to search for any morphological connection between the pulsar and the Lobe. The high quality spectral data are used to determine the evolutionary parameters of the remnant (age, shock velocity, ambient density) and to search for spectral variations within the remnant. The evolutionary parameters determined from the X-ray spectral fits provide useful constraints not only on the age and the environment in which the remnant formed but also for the pulsar. This is particularly useful for the AXP since there is no other reliable technique for estimating the age of this object (Kaspi et al. 2003; Woods et al. 2004). The detailed spectral fits of the shell and the Lobe provide useful insights into the nature of the Lobe emission. In particular, the high-quality spectra of the Lobe are used to determine if the abundances are enhanced (evidence of ejecta), if there is a nonthermal component, and if the temperature and ionization state of the plasma is similar to that of the shell.

## 2. *XMM-Newton* Data

We have observed CTB 109 with three pointings of the X-ray Multi-Mirror Mission (*XMM-Newton*, Jansen et al. 2001; Aschenbach et al. 2000) in the AO1 period covering the southern (hereafter: pointing S), northern (pointing N), and

eastern parts (pointing E). We analyze data from the European Photon Imaging Cameras (EPIC) PN (Strüder et al. 2001), EPIC MOS1, and EPIC MOS2 (Turner et al. 2001). The exposure times, after removing flares and periods of high background, are  $\sim 10$  ks. Furthermore, we have access to observation 0038140101 (PI: V. Kaspi, hereafter pointing P1), with a net integration time of 34 ks for MOS1/2. We also analyze the target of opportunity (TOO) dataset of the pulsar 1E 2259+586 in the *XMM-Newton* Archive (Obs. ID 0155350301, hereafter P2) with 17 ks of MOS2 data in full frame mode. The MOS1 was in partial window mode, covering only the pulsar. In observations P1 and P2, the PN was in small window mode. Therefore, we do not consider the PN data of the observation P1 and the PN and MOS1 data of observation P2 in our analysis. Observation details of the datasets used are listed in Table 1. Starting from the observational data files (ODFs), the data are processed with *XMM-Newton* Science Analysis System (XMMSAS) version 5.4.1. For EPIC PN, only single and double pattern events are used, whereas for the MOS1 and 2, singles to quadruples are selected.

### 2.1. Intensity Map

The SNR has been fully covered in five pointings with different directions (three for the shell and two centered on the pulsar). We therefore merge the images from the different pointings to obtain complete exposure corrected images of the remnant using the procedure `emosaic`. For all the pointings, events are selected in the energy bands:  $0.3 - 0.9\text{ keV}$ ,  $0.9 - 1.5\text{ keV}$ ,  $1.5 - 4.0\text{ keV}$ , and  $4.0\text{ keV} - 12.0\text{ keV}$ . Images are created with a bin size of  $4''$  and smoothed with circular Gaussian function that has a sigma of 3 pixels in both dimensions RA and Dec. In the  $4.0\text{ keV} - 12.0\text{ keV}$  images, only significant emission from the pulsar is seen, but not from the rest of the SNR.

Figure 1 shows a mosaic image in the energy band of  $0.3 - 4.0\text{ keV}$  in false color. The remnant's X-ray emission fades off to the west, lacking a clearly defined edge. In the interior, the Lobe is brighter than any part of the shell and there are dark regions north and south of the Lobe. The Lobe emission is well separated from the pulsar. We estimate the distance of the shell from the pulsar in the mosaic image by fitting a circle centered

on the pulsar to each sector and obtain: 18'5 for the eastern shell, 17'3 for the southern shell, and 16'6 for the northern shell. Thus, the eastern shell has the largest projected distance from the pulsar.

## 2.2. RGB Composite Image

As no emission from the remnant is found above 4 keV except from the pulsar, we create images in the energy bands below 4 keV in order to identify possible spectral variations within the remnant. The images in the bands red (R) = 0.3 – 0.9 keV, green (G) = 0.9 – 1.5 keV, and blue (B) = 1.5 – 4.0 keV are combined into an RGB mosaic image (Fig. 2). We then use this image to guide our selection of regions to be examined more closely through detailed spectral fitting. The selected regions are shown in Figure 3.

The shell is slightly redder than the interior and has some red clumps. There is a small sector of the shell with lower emission in the northeast, coinciding with a bright region in the radio continuum (Kothes et al. 2002). Next to this region, there are red knots in the RGB composite image of the X-ray shell (regions 5 and 6 in Fig. 3). Furthermore, there is a larger red spot in the south (region 15). There are also color variations within the Lobe, the outskirts being redder than the central part of the Lobe.

In addition to the very bright pulsar, fainter point sources are found in and around the remnant. Two point sources located southeast of the remnant appear red in the RGB composite image. The one further east at RA =  $23^h03^m19.6^s$ , Dec =  $+58^\circ45'29''$  (J2000.0) is a star of the spectral type G5.5:V (USNO-A2.0 1425-14515707, Monet et al. 1998) and is coincident with source No 3 in RP97. The other source at RA =  $23^h02^m43.7^s$ , Dec =  $+58^\circ37'46''$  (J2000.0) is coincident with source No 4 in RP97; it is also coincident with a point source in the DSS image. Presumably, it is also a Galactic star. The point sources close to the pulsar (in projection) have blue or violet colors. The source at RA =  $23^h00^m33.3^s$ , Dec =  $+58^\circ52'45''$  (J2000.0) located west of the pulsar is USNO-A2.0 1425-14436845 (No 1 in RP97), a star of the spectral type G9.5:III-IV. The source at RA =  $23^h00^m43.3^s$ , Dec =  $+58^\circ50'28''$  (J2000.0) south of USNO-A2.0 1425-14436845, is only known as an X-ray source (No 2 in RP97). There is an optical point source on the DSS image at the X-ray posi-

tion. Therefore, these hard point sources seem to be Galactic stars as well. Enhanced column density in the foreground or high intrinsic absorption seems to be responsible for the hard spectrum. We extracted spectra for these point sources, but the low number of counts does not allow detailed spectral fitting.

## 2.3. Background

Since CTB 109 is a relatively faint diffuse object, a good knowledge of the background is crucial for the spectral analysis. We studied the background properties of the EPIC cameras based on the treatments of Lumb (2001), Lumb et al. (2002), and Read & Ponman (2003).

In the case of a point source a local background extracted from another region of the same data as the source can be used. For extended objects, it is not possible to obtain background data at small distances from the source, i.e. a few arcseconds away from the source like for point or point-like sources. Instead one has to extract the background data far from the target, from a part of the detector that is not illuminated by source emission. In this case the distance between the source and the background region is large (few arcminutes) and the difference of the detector background at the two positions could become significant (see next paragraph). In the case of a diffuse source that fills the entire field of view, it is even impossible to estimate the local background from the same data. If one selects a background region far from the source itself, many effects can produce an inappropriate background due to the different chip position: First, the effective area of the mirrors depends on the off-axis angle. Photons are subject to vignetting, but particles are not. Second, high-energy particles which interact with material surrounding the detector produce fluorescence, the magnitude of this fluorescence emission can vary significantly with position on the detector, especially for the PN detector. Third, the spectral response depends on the position on the detector, especially for the PN.

The internal ‘quiescent’ background of the EPIC cameras consists of fluorescence lines and events produced by charged particles. The fluorescence depends on the camera body materials and the incident flux of high energy charged particles. Therefore, the fluorescent component varies

with position on the detector and with time. In addition, the high energy charged particles can produce background events directly in the detector. Finally, low energy protons can reflect off of the mirror surfaces and reach the detectors in the focal plane. The background produced by low energy protons is highly variable in time for the *XMM-Newton* instruments.

There are two types of background template files available that can be used for the analysis of EPIC data: ‘Closed’ data and blank sky data. ‘Closed’ data have been obtained with the filter wheel in the ‘closed’ position; these data include only the internal detector background. However, this instrument configuration is not representative of the usual observation where the CCDs are exposed to photons and low energy charged particles. For the blank sky data, datasets for different pointings have been merged for each EPIC camera after eliminating sources from the data. These datasets comprise the detector background and an average cosmic X-ray background. Since the background component due to high energy charged particles is included in these data at an unknown level, we need to model it using the spectral shape determined from the closed data.

## 2.4. Extraction of EPIC Spectra

### 2.4.1. Circular Regions

Although the cosmic X-ray background is a significant uncertainty in the blank sky data, we decide to use the blank sky instead of the ‘closed’ data, because the latter have poor photon statistics and are therefore not suitable for extracting small regions. We use the blank sky data of the background analysis group in Birmingham, UK <sup>1</sup>, because they have data for both the medium and the thin filters, as well as for the full frame and extended full frame PN modes. The Birmingham group have also developed scripts that can be used for the background analysis. The script `skycast` converts the detector coordinates of the template background datasets into sky coordinates using the pointing direction of the observation to be analyzed and adds sky coordinates to the background data. The script `createspectra` extracts spectra in specified circular (or annular) regions

from the data and background-file. Ancillary response files (ARFs) and redistribution matrix files (RMFs) are produced for the corresponding detector regions using the XMMASAS commands `arfgen` and `rmfgen`. Since the source spectrum and associated blank sky background spectrum are created at the same position of the detector, the ARF and RMF are correct for both source and background.

Spectra are analyzed with XSPEC Ver. 11.3. We read in the source and the blank sky background spectra as two datasets: source (1), background (2). We model the background spectrum as a combination of a powerlaw component and two Raymond & Smith (Raymond & Smith 1977, hereafter RS) components with temperatures  $kT = 0.08$  keV and 0.2 keV (Lumb 2001; Lumb et al. 2002). Zero-width Gaussians are used to reproduce the fluorescence lines of the detector. The detector background is modeled with a powerlaw component and Gaussians using the XSPEC option ‘/b’ to suppress the application of the ARF. An additional thermal component is used to model the SNR emission (set to zero for the background dataset). In Figure 4, the EPIC PN and MOS1/2 spectra of region 1 (see Fig. 3) extracted from the E pointing are displayed together with the corresponding blank sky background spectra. We show the spectrum from region 1 since this is the faintest part of the Lobe, and hence the most sensitive to the background subtraction.

In order to convince ourselves that the background in the source spectrum can be well estimated from the blank sky data, we compare the spectra extracted as source (from observations) and background (from blank sky data) in a region outside the SNR. Both for PN and for MOS1/2, the off-remnant spectrum from observations matches the blank sky spectrum very well in the softer ( $< 0.6$  keV) and harder ( $> 1.5$  keV) bands as well as for the fluorescence lines. There is a small excess in the off-remnant spectrum between  $\sim 0.6$  and 1.5 keV. This faint emission is well fitted with a thermal model component and is likely Galactic diffuse X-ray emission. Since the remnant spectrum dominates the background spectrum in the 0.6 – 1.5 keV band (see Fig. 4), using the blank sky data as background introduces only a small systematic uncertainty in the derived parameters for the remnant spectra. We verify this by modeling the spectra of regions in

<sup>1</sup>See <http://www.sr.bham.ac.uk/xmm3/>.

the remnant shell including an additional thermal component for the local diffuse X-ray background, as derived from the off-remnant spectrum. The parameters of the model component for the remnant emission (foreground absorption, temperature, and ionization timescale, see § 3) are consistent with results from the fit using only the blank sky data as background. The abundances of the elements with emission lines in this energy band (O, Ne, and Mg) also yield fit results that agree well with the results without the additional component, i.e. solar abundances. Consequently, the use of the blank sky data as background should have little effect on our determination of the neutral hydrogen column density and on the temperature of the thermal component.

#### 2.4.2. Arbitrary Extraction Region Shape

Since the existing version of `arfgen` only computes ARF files for circular and annular extraction regions, our analysis has been largely limited to circular regions. However, the XMM-SAS command `evigweight` calculates the vignetting correction for each event and thus one can use the on-axis ARF. In order to subtract the non-vignetted events from the observation data, it is better to use the ‘closed’ data for the background, as this dataset only consists of the non-vignetted component, which is the internal detector background, and thus includes no additional external background emission. Compared to the blank sky data, the ‘closed’ data have far poorer statistics. Therefore, we use this method only for non-circular extraction regions.

After computing the weight factor for the vignetting correction for each event, spectra are extracted from the new event files and RMFs are created with `rmfgen`. The source data still include the non-vignetted events which have not passed through the X-ray telescope, but now have a weighting factor applied. This misapplication of the weighting factor to non-vignetted events can be compensated for by applying the same weights to the ‘closed’ background data. Coordinates of the ‘closed’ data are converted into the corresponding sky position using `skycast`. The vignetting correction weights are computed for the ‘closed’ data. Finally, spectra are extracted in the same regions as for the observed source data. Again the background spectrum is used as second

dataset and modeled as in § 2.4.1.

#### 2.4.3. Comparison of the Two Methods

In order to check for consistency between the two methods for creating spectral data, spectra of the Lobe regions (see § 3.4), extracted from the pointing E data, are analyzed using both methods and compared. For the first method, we use the blank sky data as background data and create the ARF with `arfgen`. For the second method, the event files are vignetting-corrected with `evigweight` and on-axis ARF and ‘closed’ background data are used. All the fitted parameters derived from the two methods agree within 90% confidence limits. Therefore, we are confident that either method may be used without introducing systematic errors which dominate over the statistical errors.

### 3. The Spectral Analysis

The *XMM-Newton* EPIC data allow us to perform spatially resolved spectral analysis of the SNR. Extraction regions are shown in Figure 3 on the 0.3 – 4.0 keV mosaic image. Datasets and extraction regions are selected as follows:

- As we have shown in § 2.1, the eastern part of the shell is farthest from the pulsar. Since it is located opposite to the GMC complex in the west, the eastern shell segment most likely indicates a blast wave propagating into a lower-density ISM (Kothes et al. 2002). For the spectral analysis, we cover the eastern shell with three circular regions (7 – 9) and also arc regions for comparison. In addition, we extract spectra for regions next to the radio bright knot in the northeast (regions 5 and 6). Dataset E is used for all these analyses.
- The shell is brightest in the northern part; it has been covered completely by pointing N. We select circular regions from this dataset centered on the brighter knots (regions 12 and 13) and also analyze interior regions close to the northern shell for comparison (regions 11 and 14).
- In the southern part of the shell which does not have as clearly a defined edge as the eastern or the northern portions of the shell, we

study the EPIC spectra (using observation S) for two regions (15, 16) with soft emission (see RGB composite image, Fig. 2).

- In CO observations, an enhancement of CO gas has been found which extends from the GMC in the west across the northern part of the remnant (Tatematsu et al. 1987). This dense material is called the CO arm. Its position and shape coincides well with an X-ray faint interior region, north of the pulsar and the Lobe (see Fig. 1). Spectra are analyzed for a large circular region (10) as well as for a non-circular region which follows the shape of the very low emission region. Data from observations N and P1 are used.
- The interior of the remnant has remarkably low surface brightness in the south (‘Dark Interior’). This region is analyzed using the P1 data which have the longest exposure time.
- We extract spectra for four regions of the Lobe (regions 1 – 4 in Fig. 3) from the observations E, P1, and P2, in order to look for spectral variations.

All the EPIC spectra are analyzed in XSPEC using an energy range of 0.3 – 10.0 keV. The spectra are grouped with a minimum of 20 counts per bin and the  $\chi^2$  statistic is used. The errors quoted are 90% confidence limits. As can be seen in Figure 4, the emission above  $\sim 4$  keV is mainly background emission and is crucial for estimating the background. Although we select the energy range of 0.3 – 10.0 keV for spectral fitting, we will only show the spectrum below 4 keV in the following figures in order to clearly display the SNR emission.

For analyzing the *XMM-Newton* EPIC spectra we use the following models: VMEKAL, which describes an emission spectrum for hot ionized gas in collisional ionization equilibrium with variable abundances (Mewe et al. 1985, 1986; Kaastra 1992; Liedahl et al. 1995), and VNEI, which is a model for a non-equilibrium ionization (NEI) collisional plasma, again with variable abundances (Hamilton et al. 1983; Borkowski et al. 1994; Liedahl et al. 1995; Borkowski et al. 2001). The VNEI model includes a parameter for the ionization timescale,  $\tau = \int n_e dt$ , an integral over the time since the gas

was shocked. In addition, we modeled some regions in the shell with the model VPSHOCK for a constant temperature, plane-parallel shock which includes a range of ionization timescales, parameterized by the lower limit and the upper limit of the  $\tau$  range (Borkowski et al. 2001, and references therein).

The *XMM-Newton* EPIC spectra of region 3 in the Lobe extracted from the pointing E data (with VNEI model fits) are presented in Figure 5. Emission line features corresponding to the Mg XI triplet and the Si XIII triplet are easily visible. Moreover, the Ne X Ly $\alpha$  line can be clearly seen in the MOS data, as the energy resolution of MOS is slightly better than that of PN.

We first fit the spectra with free abundances. For all the spectra, the abundances for all the elements are consistent with solar abundances. We thereupon fix the abundances to solar values in order to reduce the number of free parameters and hopefully to better constrain the remaining free parameters. Only Mg and Si are still kept free, because these abundances have appeared to differ slightly from solar values for some regions and the line features are evident in the EPIC spectra. We allowed the Si and Mg abundances to vary independently. For other elements like Ne or S, it is too difficult to distinguish between line and continuum emission in the corresponding energy intervals.

All the EPIC spectra are fitted better by a single-temperature VNEI model than by a collisional ionization equilibrium VMEKAL model. In the following, we present only the VNEI results for all the regions, and discuss the VPSHOCK results for shell spectra where we expect the least disturbed plane-parallel shock. Tables 2 and 3 summarize the results of the spectral analysis of MOS1/2 data, using the VNEI model. Spectra of some selected regions with the best fit VNEI model are displayed in the following figures: Figure 5 shows the PN and MOS1/2 spectra of the brightest part of the Lobe (region 3), the spectra in Figure 6 are extracted from a bright region in the shell (region 5), and Figure 7 shows the heavily absorbed spectra of the CO arm. In all these plots, the non-background-subtracted source spectra are shown, but not the simultaneously modeled background spectra.

The parameters of the VNEI model for the Lobe data of the pointing E, with the spectra from the

two EPIC detector types PN and MOS fitted separately, are consistent with the MOS results of the Lobe regions in Table 2 except that the Mg and Si abundances from the PN fits turn out to be subsolar in some regions. The most likely explanation for this discrepancy between PN and MOS is the calibration issue addressed in the EPIC calibration status documentation of April 2003 (Kirsch 2003): In the range from 0.3 – 1.0 keV, the PN flux is up to 10% higher than the MOS flux, whereas above 1.5 keV, the MOS flux is up to 10% higher. In the EPIC spectra, most of the emission lines cannot be resolved due to moderate spectral resolution. This complicates the determination of the continuum. Assuming the same temperature and absorption, the flux inconsistency between the MOS and the PN can mimic lower abundances for the PN data for elements like Mg and Si with lines above  $\sim 1$  keV, because the unresolved lines cannot be distinguished from the continuum. Although most of the fit parameters (absorption, temperature, ionization timescale) for the PN, MOS1, and MOS2 spectra are consistent, the discrepancy between the abundances makes us conclude that the results from the MOS data (MOS1 and MOS2 data fitted simultaneously, if data of both instruments are available) are more reliable than the PN results in terms of abundances. Therefore, we list the MOS1/2 results in Tables 2 and 3.

### 3.1. Shell

#### 3.1.1. Eastern Part of the Shell

The eastern part of the remnant shell is farthest from the pulsar 1E2259+586 and has a more circular shape. The density of the ambient ISM is apparently lower on this side (Kothés et al. 2002). Thus the eastern portion of the shell seems to be the best region to study the least perturbed shock-ISM interaction.

The spectral analysis of regions in the eastern shell (regions 6 - 9) yields a temperature of  $\sim 0.6$  keV for the VNEI model, which is slightly higher than those in the Lobe and the northern portion of the shell, though not significantly. The Mg and Si abundances are consistent with solar, and the ionization timescale is  $\sim 1 \times 10^{11}$  s  $\text{cm}^{-3}$ , similar to that in the northern part of the shell (see § 3.1.2). The absorbing column density is  $N_{\text{H}} = 5 - 7 \times 10^{21}$   $\text{cm}^{-2}$ . We also analyze the spec-

tra of the regions in the eastern shell using the model VPSHOCK. The values for  $N_{\text{H}}$ ,  $kT$ , and the abundances agree well with the results of the VNEI model in all four regions. The lower limit of  $\tau$  has been set equal to zero. The upper limit of the ionization timescale  $\tau$  is  $3.4_{-0.3}^{+0.7} \times 10^{11}$  s  $\text{cm}^{-3}$  for region 6,  $4.8_{-2.5}^{+7.2} \times 10^{11}$  s  $\text{cm}^{-3}$  for region 7,  $3.5_{-1.7}^{+30.0} \times 10^{11}$  s  $\text{cm}^{-3}$  for region 8, and  $6.8_{-1.1}^{+10.0} \times 10^{11}$  s  $\text{cm}^{-3}$  for region 9, all higher than and therefore consistent with the average values obtained from the VNEI model.

No indication of nonthermal emission is found in these spectra. We model the spectra with an additional powerlaw component and obtain an upper limit for the flux of the powerlaw component. Studies of nonthermal emission from the shells of SNRs yield photon indices of around 2.0:  $\Gamma = 1.8$  for Cas A (below 16 keV, Allen et al. 1997) and  $\sim 2.2$  for SN 1006 (Bamba et al. 2003; Allen et al. 2004). Therefore, we assume a photon index of  $\Gamma = 2.0$  and obtain upper limits of the nonthermal flux (0.3 – 10 keV, 90% confidence level):  $1.7 \times 10^{-14}$  ergs  $\text{cm}^{-2}$   $\text{s}^{-1}$  in region 6,  $1.3 \times 10^{-13}$  ergs  $\text{cm}^{-2}$   $\text{s}^{-1}$  in region 7,  $3.0 \times 10^{-14}$  ergs  $\text{cm}^{-2}$   $\text{s}^{-1}$  in region 8, and  $1.5 \times 10^{-14}$  ergs  $\text{cm}^{-2}$   $\text{s}^{-1}$  in region 9, i.e.  $<0.2\%$ ,  $<1.6\%$ ,  $<0.4\%$ , and  $<0.2\%$  of the unabsorbed VNEI flux, respectively. Gotthelf et al. (2001) have studied the emission from the forward shock in the northern part of Cas A and report that the flux of the nonthermal emission is 50 – 70% of the total 0.5 – 10.0 keV flux. In comparison, the upper limit of the nonthermal emission from the eastern part of the shell of CTB 109 in the energy range of 0.5 – 10.0 keV is 0.2 – 1.4%, about two orders of magnitude lower than in Cas A.

In radio continuum, CTB 109 has a very bright extended region approximately where the connecting line from the pulsar through the Lobe intersects the shell in the northeast (see e.g. Fig. 1 in Kothés et al. 2002). In region 5 which lies north of this radio bright region, the column density  $N_{\text{H}}$  ( $\sim 8 \times 10^{21}$   $\text{cm}^{-2}$ ) and the ionization timescale  $\tau$  ( $6 \times 10^{11}$  s  $\text{cm}^{-3}$  from the joint fit of PN and MOS1/2 data,  $4 \times 10^{11}$  s  $\text{cm}^{-3}$  from the fit of MOS1/2 data, see Table 2) are higher compared to the eastern shell regions south of the radio bright region, whereas the temperature is significantly lower:  $kT = 0.29 \pm 0.03$  keV at the 90% level, as obtained from both the PN and MOS1/2 fit

and the MOS1/2 fit. The  $kT$  value for region 5 differs from that in other regions also at the 99% confidence level. The spectra are shown in Figure 6. Fitting a model similar to other shell spectra ( $N_{\text{H}} = 6 \times 10^{21} \text{ cm}^{-2}$ ,  $kT = 0.6 \text{ keV}$ ,  $\tau = 1 \times 10^{11} \text{ s cm}^{-3}$ ) results in a modeled spectrum with lower flux below 0.9 keV and flatter continuum above 2 keV, compared to the observed spectrum. The optical image of Fesen & Hurford (1995) shows that this region covers two bright optical filaments with a  $[\text{S II}]/\text{H}\alpha$  ratio typical for shocked gas rather than of photoionized gas; they derive a pre-shock density of  $10 - 20 \text{ cm}^{-3}$ , higher than for other optical filaments seen in CTB 109. This might indicate that a shock-cloud interaction is occurring in region 5. The ionization timescale for this region is  $\sim 4 - 6$  times higher than in other parts of the remnant shell. Since the regions are all located at similar radii, the time that has elapsed after these regions have interacted with the shock front can be assumed to be comparable. Therefore, the higher  $\tau$  in region 5 is consistent with the shock having encountered a density enhancement.

Although we assume that the undisturbed eastern part of the remnant can be reproduced by a model based on the Sedov-Taylor-von Neumann similarity solution (Sedov 1959; Taylor 1950; von Neumann 1947), the fit results are not satisfactory if we use the SEDOV model (Borkowski et al. 2001) in XSPEC. This is presumably due to inhomogeneities in the ISM that result in flux and spectral variations in the remnant. Therefore, we focus on smaller shell segments and analyze arc-shaped regions of the eastern shell (see Fig. 3 and Table 3) using the `evigweight` method. As the VNEI fit results show, the spectra in the ‘outer’ and ‘inner’ shell seem to be different: The best fit temperature is slightly higher in the outer shell, whereas the ionization timescale is lower. The foreground absorption is lower for the outer shell than for the inner shell. However, if we compare the confidence contours of  $N_{\text{H}}$  vs.  $kT$  and  $kT$  vs.  $\tau$  for the two shell regions, the 90% confidence regions are fully separated, but the 99% regions overlap. Thus, there is only a marginal inconsistency between the temperatures and the ionization timescales of the outer shell and the inner shell.

For a Sedov-phase remnant expanding into a homogeneous medium, the temperature and ion-

ization timescale both increase radially inward. This is an idealized case, however. If the  $kT$  and  $\tau$  differences are real, we may be seeing the effects of nonuniformities in the ambient medium. If the shock (as seen in projection) encountered a density enhancement, that could cause a larger ionization timescale and lower temperature, and reduce the flux in the inner shell region relative to the outer shell region.

### 3.1.2. Northern Part of the Shell

For the northern portion of the shell (regions 12, 13)  $N_{\text{H}} \approx 7 \times 10^{21} \text{ cm}^{-2}$ ,  $kT \approx 0.5 \text{ keV}$ , and  $\tau \approx 1 \times 10^{11} \text{ s cm}^{-3}$ . The temperature seems to be lower and the column density  $N_{\text{H}}$  higher than in the eastern portion of the shell. For regions inside the northern shell segment (regions 11, 14), the column density  $N_{\text{H}}$  seems to be slightly higher ( $8 - 9 \times 10^{21} \text{ cm}^{-2}$ ), perhaps indicating a gradual increase of the foreground absorption in the direction of the CO arm.

### 3.1.3. Southern Part of the Shell

In the southern portion of the shell, there are two diffuse spots that appear red in the RGB composite image (Fig. 2): a bright region in the south-east (region 15) and the western tip of the shell in the south (region 16). The temperature is 0.6 keV and the ionization timescale  $\tau \approx 1 \times 10^{11} \text{ s cm}^{-3}$ , comparable to the eastern part of the shell. Rather than being a result of a lower temperature plasma, the red color of these regions appears to be a result from a lower  $N_{\text{H}}$  ( $\sim 5 \times 10^{21} \text{ cm}^{-2}$ , as derived from a joint fit of PN and MOS1/2 data,  $\sim 5.5 \times 10^{21} \text{ cm}^{-2}$ , from MOS1/2 data only).

## 3.2. CO Arm

We analyze a circular region covering the extended tip of the CO arm (region 10). The column density  $N_{\text{H}}$  is higher than in the eastern part of the shell and the Lobe,  $N_{\text{H}} > 8 \times 10^{21} \text{ cm}^{-2}$ , but the temperature, the Mg and Si abundances, and the ionization timescale are comparable to the shell of the remnant ( $kT = 0.5 - 0.6 \text{ keV}$ ,  $\tau = 1 - 2 \times 10^{11} \text{ s cm}^{-3}$ , as derived from PN and MOS1/2 data).

We also study a non-circular X-ray faint region corresponding to the CO arm (see Fig. 3), using `evigweight`. Figure 7 shows the spectra of this

region obtained with the EPIC MOS1/2 of the pointing P1; the flux falls off more rapidly below 1 keV compared to other regions of the SNR, consistent with the presence of additional absorption. The result of the spectral fit of the MOS1/2 data is given in Table 3; it confirms that the column density  $N_{\text{H}}$  is almost  $10^{22} \text{ cm}^{-2}$ , higher than in other regions of the remnant. The intrinsic spectrum seems to be the same as in most of the other regions of the remnant. Therefore, we conclude that this region appears fainter because of additional absorption.

### 3.3. Dark Interior

There is a low surface brightness region south of the Lobe inside the remnant shell. No enhanced CO emission is found in the observations by Tatematsu et al. (1990) that coincide with this X-ray faint region. We extract the X-ray spectrum of this region using the `evigweight` method excluding the point source which is located within this region. The parameters  $kT$ , Mg and Si abundances, and  $\tau$  of the dark region are all consistent with the parameters of the CO arm (Table 3), indicating that the intrinsic spectra of these two regions are similar. Only the column density  $N_{\text{H}}$  is higher in the CO arm. The spectral parameters also agree well with the parameters of region 1 (northern tip of the Lobe) which has about the same distance to the pulsar as this region. Although  $N_{\text{H}}$  does not differ significantly from that in region 1, it seems to be higher in this dark region, indicating a higher absorption.

### 3.4. Lobe

There are three observations which we can use to study the Lobe: pointings E, P1, and P2. The results from pointings E and P2 are consistent with that from pointing P1. The largest number of counts is obtained from the observation P1, because the exposure time is 2 to 3 times longer than in other observations. We also fit all the spectra (PN and MOS1/2 data of pointing E, MOS1/2 data of pointing P1, and MOS2 data of pointing P2) simultaneously for each of the regions 1 – 4. The results of these simultaneous fits are all consistent with the results of the fit of the MOS 1/2 data of pointing P1 (shown in Table 2).

In all the Lobe regions, the best fit tempera-

tures,  $kT$ , range from 0.53 to 0.59 keV (from simultaneous fit of PN and MOS1/2 as well as from the fit of MOS1/2 data, see Table 2). For Lobe regions 2 – 4, the column density  $N_{\text{H}} \approx 5 \times 10^{21} \text{ cm}^{-2}$  and the ionization timescale  $\tau = 2 - 3 \times 10^{11} \text{ s cm}^{-3}$ . The rather small differences in temperature, ionization timescale, and  $N_{\text{H}}$  seem to be responsible for the apparent spectral differences seen as color variations in the RGB composite image (Fig. 2). But the detailed spectral analysis indicates that there are no statistically significant differences among the four regions. In the bright central part of the Lobe, Si appears to be slightly overabundant ( $1.6 \pm 0.2$  times solar), while the Mg abundance is consistent with solar. This is not what we would expect if the by-products of dust destruction were contributing to the X-ray emitting material, because the Mg and Si abundances should track each other (Itoh 1989; Vancura et al. 1994, and references therein). Since the other three regions have Si abundances consistent with solar and all regions have Mg abundances consistent with solar, there is no compelling evidence for ejecta material in these regions. Furthermore, the global NEI fits that have all other elemental abundances set to solar values produce good fits with no large residuals around elemental emission lines.

#### 3.4.1. Line Emission Analysis

All the EPIC spectra for the Lobe show line features which can be attributed to Mg XI, Mg XII, and Si XIII lines, whereas the Si XIV line is too faint to be visible. Therefore, we use the Mg XI triplet and Mg XII Ly $\alpha$  line as line diagnostics of the NEI conditions of the plasma. We analyze the Lobe spectra from MOS1/2 data of pointing P1 and from MOS2 data of pointing P2. The spectrum is modeled using a modified ‘APEC’ (Smith et al. 2001) model that excludes all emission lines<sup>2</sup> for the continuum and Gaussians for the lines, over the energy range of 1.15 – 3.0 keV. The fitted parameters for the Gaussians are used to determine the line centroids and fluxes. The line energies for the Gaussians are modeled as follows: 1.211 keV for Ne X Ly $\beta$ ,  $\sim$ 1.340 keV for Mg XI triplet, 1.472 keV for Mg XII Ly $\alpha$ ,  $\sim$ 1.850 keV for Si XIII triplet, and  $\sim$ 2.440 keV for S XV.

With the spectral resolution of the EPIC de-

<sup>2</sup>Contact R. Smith for a copy of this model.

tectors, we are not able to resolve the lines in the Mg XI triplet. Therefore, we model the Mg XI line feature with one Gaussian and determine the line centroid. Variations in the line centroid from region to region would be indicative of different relative strengths of the resonance, intercombination, and forbidden lines. However, the line centroids of Mg XI are equal for all four Lobe regions within the 90% confidence intervals (Table 4). The data simply are not of high enough quality to determine such a small shift. However, the EPIC spectral resolution is sufficient to resolve the Mg XI triplet from the Mg XII Ly $\alpha$  line. From the fluxes of the Mg line complexes, the ratio Mg XI triplet/Mg XII Ly $\alpha$  is calculated. In Table 4, the line energy in keV and the flux in photons/cm<sup>2</sup>/s/extraction area are given for the Mg XI triplet and the Mg XII Ly $\alpha$  line, as well as the derived ratio of Mg XI triplet/Mg XII Ly $\alpha$ .

The resulting lines fluxes and line ratios are compared to NEI plasma models obtained using `neiline` (see Appendix A). The calculation provides line emissivities for different temperatures and ionization timescales. In Figure 8, the Mg XI triplet/Mg XII Ly $\alpha$  line ratio of region 3 for P1 data derived from the spectral analysis and error estimate based on the 90% confidence intervals for the line fluxes is plotted as a function of the ionization timescale  $\tau$  and temperature  $kT$ . We also plot the best fit values from the global VNEI fit for  $kT$  and  $\tau$  and the 90% errors. Since region 3 has the best statistics, it gives the narrowest band in the  $kT$ - $\tau$  diagram. Within the errors, the VNEI value lies within the allowed region resulting from the line ratio analysis. From the diagram, we can derive the  $kT$  range for region 3 as:  $kT > 0.32$  keV. This lower limit is consistent with the results from the VNEI fit of the EPIC spectra in the total energy range of 0.3 – 10.0 keV (Table 2). The ratio of the Mg XI triplet to Mg XII Ly $\alpha$  does not provide a constraint on the ionization timescale.

These results show that line diagnostics are possible with CCD spectra. Compared to global fits, they suffer from fewer systematic uncertainties, while it is difficult to quantify the systematic errors of global fits. Line diagnostics are independent of foreground absorption and offer an additional method to constrain the plasma parameters. In our analysis the spectral resolution and the photon statistics only allow to set a lower limit on

the temperature. However, the results obtained from fitting the lines only and from fitting the entire EPIC spectrum are consistent with each other. This method is a promising technique of analyzing plasma conditions and can be applied for brighter SNRs as well as for future missions with higher spectral resolution and larger collecting area.

### 3.4.2. Nonthermal Emission

In order to check if there is nonthermal emission from the Lobe that would be associated with a pulsar jet, we fit the spectra of regions 1 – 4 in the energy range of 0.3 – 10.0 keV with a model including a VNEI component and an additional powerlaw component for the Lobe emission. The fit does not improve significantly, and the flux of the powerlaw component is consistent with zero. Therefore, we derive an upper limit for the flux of the powerlaw component, assuming a photon index of  $\Gamma = 1.5$ ; typical photon indices for pulsar jets are  $\sim 1.2 - 1.7$  (Lu et al. 2002; Gaensler et al. 2002; Pavlov et al. 2003). The nonthermal flux of the Lobe (0.3 – 10 keV) is  $< 9.2 \times 10^{-15}$  ergs cm<sup>-2</sup> s<sup>-1</sup> in region 1 (90% confidence level),  $< 8.0 \times 10^{-15}$  ergs cm<sup>-2</sup> s<sup>-1</sup> in region 2,  $< 7.0 \times 10^{-15}$  ergs cm<sup>-2</sup> s<sup>-1</sup> in region 3, and  $< 6.1 \times 10^{-15}$  ergs cm<sup>-2</sup> s<sup>-1</sup> in region 4, i.e.  $< 0.05\%$ ,  $< 0.08\%$ ,  $< 0.05\%$ , and  $< 0.07\%$  of the unabsorbed VNEI flux in regions 1 – 4, respectively. For the entire Lobe, the upper limit for the nonthermal emission is  $6.9 \times 10^{-14}$  ergs cm<sup>-2</sup> s<sup>-1</sup>, corresponding to  $8.2 \times 10^{-6}$  photons keV<sup>-1</sup> cm<sup>-2</sup> s<sup>-1</sup> at 1 keV. For comparison, the intensity of the Vela pulsar jet is  $\sim 4 \times 10^{-5}$  photons keV<sup>-1</sup> cm<sup>-2</sup> s<sup>-1</sup> at 1 keV (Pavlov et al. 2003).

## 4. Estimates Based on the Sedov Solution

The morphology of CTB 109 and the existence of the giant molecular cloud complex in the west suggests that the shock wave expanded into a dense cloud and decelerated very quickly. To the east, the shock wave is expanding into a lower-density medium. CTB 109 seems to be confined by denser material in the north and the south (Fesen & Hurford 1995), which might be responsible for the smaller radii of the northern and the southern X-ray shells compared to that of the eastern shell (§ 2.1). However, the difference is relatively small ( $\sim 5 - 10\%$ ) and overall the X-ray shell of

CTB 109 can be considered as a semi-circle. Calculations for the evolution of SNRs adjacent to a molecular cloud show that the shock propagation on the low-density side is almost unaffected by the presence of the molecular cloud (e.g. Tenorio-Tagle et al. 1985; Wang et al. 1992) and can be modeled as a spherical problem. The X-ray temperature of  $\sim 3 - 8 \times 10^6$  K and the bright and well-defined X-ray rim of the remnant, as well as the lack of optical emission except in a few particular regions with higher density, indicate that the remnant has not yet reached the radiative phase. To estimate physical parameters for the remnant, we apply the shock jump conditions and the Sedov-Taylor-von Neumann similarity solution (Sedov 1959; Taylor 1950; von Neumann 1947). We assume a distance,  $D$ , to CTB 109 of  $3.0 \pm 0.5$  kpc as estimated by Kothés et al. (2002), and introduce a scaling factor  $d_3 = D/3.0$  kpc. For the mass and densities, the following relations apply: Assuming cosmic abundances (Anders & Grevesse 1989), the gas density (excluding electrons) is  $n = 1.1 n_{\text{H}}$ , where  $n_{\text{H}}$  is the atomic H number density. The electron number density depends on the ionization state of the gas; if we assume at least single ionization for each element,  $n_e = (1.1 - 1.2) n_{\text{H}}$ , and the total number density, including electrons, is  $n_{\text{tot}} = n_e + n = (2.2 - 2.3) n_{\text{H}}$ . The corresponding mass per free particle is  $\bar{m} = (0.64 - 0.61) m_{\text{p}}$ , with proton mass  $m_{\text{p}} = 1.67 \times 10^{-24}$  g. The mean mass per nucleus in any ionization stage is  $\bar{m}_{\text{n}} = 1.4 m_{\text{p}}$ . In the following, suffix ‘0’ denotes pre-shock values, and suffix ‘s’ denotes post-shock values.

For the radius of the blast wave, we use the distance of the eastern shell from the pulsar as estimated from the EPIC image:  $R_s = 18'5 \pm 1'0 = (16 \pm 1) d_3$  pc  $= (5.0 \pm 0.3) \times 10^{19} d_3$  cm. If a supernova occurs near a molecular cloud, the shock can be reflected at the cloud surface and cause the center of divergence of the velocity field to move away from the cloud (Tenorio-Tagle et al. 1985). The pulsar might also have a proper motion. Consequently, in the case of CTB 109 the distance of the eastern part of the shell to the pulsar is only an estimate of the radius. An alternative way to estimate the radius of the remnant is to measure the half of the extent of the shell in the north-south direction. However, as there is dense matter both north and south of the remnant that might interact with the shock front, the north-south extent

rather provides a lower limit for the size of the remnant.

For the temperature, we use the result from the VNEI fits of the spectra in regions 7 to 9. The weighted mean of the temperature are calculated from the results which have been obtained by fitting the PN and MOS1/2 spectra separately, and from the results of the simultaneous fits of the PN and MOS1/2 spectra. As the comparison of these results with the values for the eastern shell (Table 3) show, there is a discrepancy of  $\lesssim 0.08$  keV between the average temperature derived from the circular regions and the temperature obtained for the outer shell. To allow for the variation between the  $kT$  estimates, we increase the error estimate to 0.10 keV for this calculation, and obtain for the temperature of the eastern part of the remnant shell:  $T_X = 0.62 \pm 0.10$  keV  $= (7.2 \pm 1.2) \times 10^6$  K.

At the discontinuity of the shock front, the density jump is  $n = 4 n_0$ , with  $n_0$  being the pre-shock ambient density of nuclei. Inside the shock front, the density decreases towards the center because of the adiabatic expansion of the remnant (Heiles 1964; Cox & Anderson 1982). In order to derive further parameters, we use the distribution of the normalized density of the nuclei,  $n(R)/n_0 = n_{\text{H}}(R)/n_{\text{H},0}$ , as calculated by Cox & Anderson (1982) and compute the emissivity numerically. The emitting volume is modeled as a cylinder intersecting a spherical remnant with the long axis of the cylinder running along the line of sight through the remnant. The radius of the cylinder is simply the radius of the extraction region which, in this case, is  $r = 80'' = 1.2 d_3$  pc for  $D = 3.0 d_3$  kpc.

From the spectral fits of the EPIC data of regions 7 to 9 with the VNEI model, we derive the normalization in XSPEC as  $K = \frac{10^{-14}}{4\pi D^2} \times \int 1.2 n_{\text{H},s}^2 dV = (1.6 \pm 0.5) \times 10^{-3} \text{ cm}^{-5}$ . Since the integral of the normalized density  $n(R)/n_0$  over the volume can be calculated numerically, the ambient ISM density  $n_0$  is estimated from the normalization  $K$ :

$$K = \frac{1.2 \times 10^{-14} n_{\text{H},0}^2}{4\pi D^2} \int \left( \frac{n_{\text{H}}}{n_{\text{H},0}} \right)^2 dV. \quad (1)$$

The projected volume is  $V = 42 d_3^3$  pc<sup>3</sup>, and the integral is  $\int (n_{\text{H}}/n_{\text{H},0})^2 dV = 240 d_3^3$  pc<sup>3</sup>. Thus the pre-shock H density is  $n_{\text{H},0} = (0.14 \pm$

0.02)  $d_3^{-0.5} \text{ cm}^{-3}$ , and the pre-shock density of nuclei  $n_0 = 1.1 n_{\text{H},0} = (0.16 \pm 0.02) d_3^{-0.5} \text{ cm}^{-3}$ .

In the case of full equilibration between the electrons and the nuclei, the shock velocity is related to the post-shock temperature as:

$$T_{\text{X}} \approx T_{\text{s}} = \frac{3\bar{m}}{16k} v_{\text{s}}^2, \quad (2)$$

where  $k = 1.38 \times 10^{-16} \text{ ergs K}^{-1}$  is the Boltzmann's constant. With a mean mass per free particle of  $\bar{m} = 0.61 m_{\text{p}}$  for a fully ionized plasma, the shock velocity is estimated as  $v_{\text{s}} = [(16kT_{\text{X}})/(3 \times 0.61m_{\text{p}})]^{\frac{1}{2}} = 720 \pm 60 \text{ km s}^{-1}$ .

It is possible that the electrons and ions are not fully equilibrated in the shock, in which case, the ion temperature  $T_{\text{ion}}$  may be higher, and the electron temperature  $T_{\text{e}}$  much lower than the mean plasma temperature  $T \approx T_{\text{ion}}$ . The electrons and ions would then equilibrate slowly through Coulomb collisions. The plasma X-ray emissivity depends primarily on the electron temperature, and the deduced velocity would be larger. Ghavamian et al. (2003) and Rakowski et al. (2003) have analyzed the blast wave of the SNR DEM L71 in the Large Magellanic Cloud and find values for  $T_{\text{e}}/T_{\text{ion}}$  at different locations ranging from 0.01 (almost no equilibration) to 1.0 (full equilibration). The evolution of the electron temperature and its ratio to the mean post-shock temperature in two-fluid phase SNR shocks has been studied by Itoh (1978). Applying the Sedov similarity solution to the energy equation and the equation of state for the electron gas and assuming Coulomb interactions between the electron and the ion gas, he shows that the ratio  $g = T_{\text{e}}/T$  is a function of a reduced time variable  $\nu = t_3(n_0^8/E_{51}^3)^{1/14}$  which describes the thermal structure of the blast wave;  $t_3$  is the time elapsed since the explosion (in units of  $10^3 \text{ yr}$ ),  $n_0$  the pre-shock density of the nuclei (in units of  $\text{cm}^{-3}$ ), and  $E_{51}$  is the initial blast energy (in units of  $10^{51} \text{ ergs}$ ). From X-ray measurements one obtains the X-ray temperature,  $T_{\text{X}}$ , the ambient density,  $n_0$ , and the radius,  $R_{\text{s}}$  of the SNR. Since these three values are related to each other as  $f = T_{\text{X}}/T = 0.043T_{\text{X}}(R_{\text{s}}n_0)^{-1/2}\nu^{7/5}$ , Itoh (1978) derives the value of  $f = T_{\text{X}}/T$  from the intersection of the curve  $f(\nu)$  with the theoretical curve for Coulomb equilibration  $g(\nu) = T_{\text{e}}/T$ . Based on this method, we determine a lower limit for the

ratio  $T_{\text{e}}/T_{\text{s}} \approx T_{\text{X}}/T_{\text{s}} \approx 0.4$ , and an upper limit for the velocity  $v_{\text{s}} = [(16kT_{\text{X}})/(3 \times 0.4 \times 0.61m_{\text{p}})]^{\frac{1}{2}} = 1140 \pm 90 \text{ km s}^{-1}$ .

The age of the remnant can be estimated from the shock velocity using the similarity solution:

$$v_{\text{s}} = \dot{R}_{\text{s}} = \frac{2R_{\text{s}}}{5t}. \quad (3)$$

Under the assumption of full equilibration of electron and ion temperatures, this yields an age estimate of  $t = (2.8 \pm 0.3) \times 10^{11} d_3 \text{ s} = (8.8 \pm 0.9) \times 10^3 d_3 \text{ yr}$ . If equilibration in the shock is incomplete, the age estimate would be lower. For the lower limit of  $T_{\text{e}}/T_{\text{s}} = 0.4$ , the age would be  $t = (1.8 \pm 0.2) \times 10^{11} d_3 \text{ s} = (5.6 \pm 0.6) \times 10^3 d_3 \text{ yr}$ .

We estimate the initial energy of the explosion from

$$R_{\text{s}} = \left( \frac{2.02E_0t^2}{\bar{m}_{\text{n}}n_0} \right)^{\frac{1}{5}}, \quad (4)$$

where the mean mass of the nuclei is  $\bar{m}_{\text{n}} = 1.4 m_{\text{p}}$ . Solving for  $E_0$  gives  $E_0 = \frac{1}{2.02} R_{\text{s}}^5 \bar{m}_{\text{n}} n_0 t^{-2} = (7.4 \pm 2.9) \times 10^{50} d_3^{2.5} \text{ ergs}$ , assuming full equilibration between the electrons and ions, and  $E_0 = (18.5 \pm 7.3) \times 10^{50} d_3^{2.5} \text{ ergs}$ , assuming partial equilibration with a lower limit of the temperature ratio of  $T_{\text{e}}/T_{\text{s}} = 0.4$ . The mass swept up by the SNR shock wave is  $M = \frac{4\pi}{3} R_{\text{s}}^3 1.4 m_{\text{p}} n_0 = (97 \pm 23) d_3^{2.5} M_{\odot}$  if we assume a uniform ambient medium.

Wang et al. (1992) have numerically modeled an SNR next to a dense molecular cloud, using the Kompaneets (1960) approximation. They obtain a geometry comparable to that of CTB 109,  $1.3 \times 10^4 \text{ yr}$  after the explosion in an interstellar medium with a density of  $n_0 = 0.13 \text{ cm}^{-3}$ . This value for the ambient density agrees well with the result we obtain from the *XMM-Newton* data. The assumed initial energy is  $E = 3.6 \times 10^{50} \text{ ergs}$ , 2 to 5 times lower than the energies we derive in our calculations. Consequently, the age estimate of Wang et al. (1992) is higher.

Rho & Petre (1997) have fitted a two-temperature Raymond & Smith model to the *ROSAT* PSPC spectrum of the northern shell, but the eastern shell is well fitted with a single temperature model with a relatively low temperature of  $kT = 0.21_{-0.04}^{+0.05} \text{ keV}$ . They derive a shock velocity of  $v_{\text{s}} = 380 \text{ km s}^{-1}$ , which is much lower than the EPIC result, and a remnant age of  $1.9 \times 10^4 \text{ yr}$  assuming a distance of 4 kpc. This age is 2 – 4

times higher than our estimate. If we assumed a larger distance of 4 kpc, the calculation for the full equilibration case would yield  $1.2 \times 10^4$  yr.

## 5. Discussion

### 5.1. X-ray spectrum

*ROSAT* PSPC and Broad Band X-Ray Telescope (*BBXRT*) spectra of CTB 109 have been analyzed Rho & Petre (1997). Assuming non-equilibrium ionization, they derive  $kT = 1.7$  keV and  $n_e t = 1.4 \times 10^{10} \text{ cm}^{-3} \text{ s}$  for the southern part of the remnant. A fit of the Lobe spectrum with a two-component Raymond & Smith model yields  $kT_{\text{low}} = 0.16^{+0.03}_{-0.04}$  keV and  $kT_{\text{high}} = 0.56^{+0.20}_{-0.10}$  keV. Their estimate for the column density,  $N_{\text{H}}$ , for foreground absorption is  $9.2^{+1.0}_{-1.5} \times 10^{21} \text{ cm}^{-2}$ . No spectral lines can be resolved in the *ROSAT* PSPC spectrum, whereas the improved spectral resolution of *XMM-Newton* EPIC allows lines to be identified, and the continuum can also be better determined. Therefore, with the *XMM-Newton* EPIC data we can show that the emission is arising from a plasma out of ionization equilibrium and also determine the temperature more accurately. In contrast to the *ROSAT* results, we obtain a good fit of the EPIC spectra of the Lobe with a single NEI model with a temperature comparable to that of the high temperature component of Rho & Petre (1997). The column density  $N_{\text{H}}$  of the EPIC fit is lower than that from the *ROSAT* data ( $\sim 5 \times 10^{21} \text{ cm}^{-2}$ ). Presumably, the lower spectral resolution data of *ROSAT* PSPC allowed successful fits to two equilibrium plasma models, but with a higher absorbing column density.

Parmar et al. (1998) have fitted the *BeppoSAX* LECS spectrum of the whole remnant shell with a non-equilibrium ionization model and obtain  $kT = 0.95^{+0.65}_{-0.27}$  keV,  $n_e t = 3.8^{+3.8}_{-1.6} \times 10^{11} \text{ cm}^{-3} \text{ s}$ , and  $N_{\text{H}} = 6.9^{+0.7}_{-1.2} \times 10^{21} \text{ cm}^{-2}$ . The analyzed spectrum does not include the emission from the pulsar and the Lobe, but encompasses the rest of the remnant. The large errors of the fit parameters of the *BeppoSAX* spectrum are presumably caused by the lower spectral resolution compared to *XMM-Newton* EPIC as well as the large extraction region including emission from various parts of the SNR.

For the *XMM-Newton* EPIC data of CTB 109, we use an NEI model for a collisional plasma with

variable abundances for Mg and Si, while fixing the abundances of other elements to solar values. In the shell and in the Lobe, the temperature is  $kT = 0.50 - 0.70$  keV, the ionization timescale  $\tau \approx 1 - 3 \times 10^{11} \text{ s cm}^{-3}$ , and the column density  $N_{\text{H}} = 5 - 7 \times 10^{21} \text{ cm}^{-2}$ , with the exception of region 5 in the northeastern shell, where the temperature is low ( $\sim 0.3$  keV) and the ionization timescale is high ( $4 - 6 \times 10^{11} \text{ s cm}^{-3}$ ). In the region corresponding to the CO arm, the absorption seems to be higher with  $N_{\text{H}} = (1.0 \pm 0.1) \times 10^{22} \text{ cm}^{-2}$ , indicating that there is additional material along the line of sight to the SNR. Abundances are consistent with solar values in the whole remnant, except for one region (the bright central region of the Lobe), where Si appears to be overabundant ( $\sim 1.6 \pm 0.2$  times solar). Since this marginal indication of overabundance is obtained only for Si in one region within the Lobe, while all the other abundances are consistent with solar, we conclude that there is no compelling evidence for ejecta emission. Given the large intensity variations within the remnant, it is somewhat surprising that none of the brighter regions shows evidence of enhanced abundances. It may be the case in CTB 109 that the ejecta mass is relatively low and the current amount of swept-up matter is relatively high such that the ejecta will be difficult to detect. Although X-ray emission from ejecta is generally observed in SNRs up to an age of a few  $10^3$  yr, there are remnants younger than CTB 109 which show no evidence for ejecta. For example, Kes 79 is estimated to be  $\sim 6000$  yr old and has no obvious emission from ejecta (Sun et al. 2004).

### 5.2. Interaction Between the SNR and the Giant Molecular Cloud

As Tatematsu et al. (1985) have shown, the CO emission stretches from the giant molecular cloud both north and south of CTB 109. In the optical band, filamentary structures have been found that are located at the rim of faint H II regions north and southeast of the SNR. At the position of the filaments, the H II regions overlap with the remnant in projection. This suggests that the optical emission is mainly caused by the interaction of the remnant with dense material harboring the H II regions (Fesen & Hurford 1995). The diffuse H II regions are probably associated with the outskirts of the molecular cloud complex to the west.

From [S II] line ratios, Fesen & Hurford (1995) derive pre-shock cloud densities of up to  $\sim 20 \text{ cm}^{-3}$  for the optical filaments. New HI and CO data (Kothes et al. 2002) make it clear that the remnant is located in a density gradient: very high density in the molecular cloud in the west and low density in the emission gap in the east of the SNR. As Kothes et al. (2002) point out, the HI map indicates that the SNR is not expanding inside a stellar wind bubble, since there is no evidence for a lower density cavity in HI with a pronounced rim.

Tenorio-Tagle et al. (1985) have performed two-dimensional numerical hydrodynamical calculations for the evolution of a supernova remnant in or near a molecular cloud. If a supernova with an initial energy of  $E \approx 10^{51}$  ergs occurs in a low density interstellar medium ( $1 \text{ cm}^{-3}$ ), the remnant shell becomes radiative after  $\sim 5 \times 10^4 - 10^5$  yr when it has reached a radius of  $R \approx 30$  pc. However, if the explosion occurs in a molecular cloud which has a higher density ( $10^3 \text{ cm}^{-3}$ ), the Sedov phase is shorter ( $\sim 10^3$  yr) and  $R$  smaller ( $\sim 1 - 6$  pc, Shull 1980; Tenorio-Tagle et al. 1985; Chevalier 1999). In the case of a supernova explosion inside a molecular cloud, a break-out occurs if the shock reaches the edge of the cloud. For CTB 109, the position of the pulsar and the shell relative to the GMC complex as well as the semi-circular shape of the shell indicate that the supernova explosion was presumably located outside and close to a giant molecular cloud. As Tenorio-Tagle et al. (1985) make clear in their calculations, a reflected shock forms from the cloud surface if the explosion takes place outside the cloud, but the shock transmitted into the cloud is weak and has a minor effect on the cloud surface. The reflected shock can cause an additional velocity component to the expansion of the SNR, directed away from the cloud. Wang et al. (1992) have modeled CTB 109 as a supernova explosion near (2 pc) a large molecular cloud, assuming an initial energy of  $E = 3.6 \times 10^{50}$  ergs, an interstellar medium density of  $n_0 = 0.13 \text{ cm}^{-3}$ , and a cloud density of  $n = 36 \text{ cm}^{-3}$ . They reproduce a semi-circular shell of the observed size at the age of  $1.3 \times 10^4$  yr.

The deep EPIC mosaic image of CTB 109 confirms that there is no emission in the western part of the remnant. In combination with the morphol-

ogy of the remnant in the radio, this indicates that the shock wave has been stopped completely in the west. However, no indication has been found for a molecular shock in the GMC (Koralesky et al. 1998, and references therein). It is possible that there is enough material in unshocked parts of the GMC which lie in front of the interaction region such that any emission from this region could be absorbed. Hard point sources discovered in the X-ray faint parts of the SNR (§ 2.2) also suggest the existence of absorbing material in front of the SNR.

### 5.3. Lobe as Shocked Cloud

Our analysis of the *XMM-Newton* EPIC data shows that the spectral properties of the Lobe are very similar to those of the remnant shell. Moreover, the merged *XMM-Newton* image (Fig. 1) corroborates that the Lobe and the pulsar are not related morphologically, confirming that the Lobe is not a jet phenomenon. Rho & Petre (1997) have suggested that, due to the interaction between the SNR and the GMC in the west, a reflected shock has propagated into the SNR. Rayleigh-Taylor instabilities might have formed between the thin SNR plasma and the dense GMC, possibly producing a structure such as the Lobe. Another possibility is that there are denser clouds in the outer parts of the GMC complex that have been shocked by the SNR blast wave. In projection, the Lobe and the bright knots in the northern part of the remnant seem to trace the outer boundary of the CO arm, and therefore might be emission from shocked interstellar clouds on the outskirts of the GMC complex.

Tatematsu et al. (1990) point out that a density fluctuation in the pre-shock gas might have resulted in a local excess of the post-shock emission measure seen as the Lobe. They estimate that a cloud with a density 2 – 5 times higher than the average pre-shock density in the ambient medium could have produced the Lobe. However, they find no evidence of CO gas accelerated by the SNR shock wave. In the far-infrared, Coe et al. (1989) have found a region with bright emission northeast of the Lobe. This region also coincides with the eastern edge of the CO arm extending from the western molecular cloud complex, which suggests that this emission is caused by a shocked cloud. Fesen & Hurford (1995) have found optical fila-

ments at the southwestern edge of the Lobe, i.e. closer to the center of the remnant. All the other optical filaments detected in their observations are located along the northern and southern shell of the remnant and seem to be the result of the SNR interacting with material associated with the H II regions in the north and the south. Usually, optical filaments are believed to be thin, shocked regions tangent to the line of sight. Since the diffuse optical emission in the north extends southward to the position of the Lobe, they suggest that the central filamentary emission arises from shocked gas along the projected edge of an interstellar cloud. Assuming a shock velocity of  $100 \text{ km s}^{-1}$ , the observed [S II] line ratio corresponds to a pre-shock cloud density of  $n_{\text{cloud}} = 5 \text{ cm}^{-3}$  (Fesen & Hurford 1995).

The interaction between a shock wave and a density enhancement like an interstellar cloud has been studied theoretically by many authors. Two-dimensional hydrodynamical calculations give information about the dynamical evolution of an interaction between the SNR blast wave and a dense cloud (e.g. Bedogni & Woodward 1990; Mac Low et al. 1994; Klein et al. 1994). The cloud fragments due to the interaction. This is also observed in three-dimensional simulations by Xu & Stone (1995), who in addition show that the morphology of the cloud after the interaction depends strongly on the initial shape of the cloud. Klein et al. (2003) have performed a laboratory experiment using the Nova high energy density laser at Lawrence Livermore National Laboratory in order to study the interaction of a shock wave with a high-density sphere located in a low-density medium. They confirm that the evolution of the sphere after the interaction depends on the density ratio of the high-density to low-density medium,  $\chi$ , and the Mach number of the shock wave, as shown by Klein et al. (1994). The high-density sphere ( $\chi = 10$ ) is destroyed by the interaction with a shock wave with a Mach number of 10.

In order to better understand the possible origin of the Lobe emission in CTB 109 we estimate cloud densities from the results of *XMM-Newton* observations based on analytical estimates by Sgro (1975) for a planar shock-cloud interaction: There are two limiting cases, the ‘cold’ cloud case and the ‘hot’ cloud case, depending on the cooling time scale in the post-shock cloud gas relative to the

crossing time for the transmitted cloud shock. A critical density is estimated by equating the cooling time and the shock crossing time:

$$n_{\text{crit}} = 5.8 \times 10^{-4} \beta^{\frac{5}{7}} v_s^{\frac{10}{7}} n_0^{\frac{5}{7}} a^{-\frac{2}{7}}, \quad (5)$$

where  $\beta$  is the ratio of the pressure behind the transmitted cloud shock and the pressure in the shocked ambient ISM,  $v_s$  the shock velocity (in  $\text{km s}^{-1}$ ),  $n_0$  the ambient pre-shock density (in  $\text{cm}^{-3}$ ), and  $a$  the size of the cloud (in pc). For a density contrast of  $\chi = n_{\text{cloud}}/n_0 = 10, 100$ , and  $\infty$ ,  $\beta$  is 2.6, 4.4, and 6.0, respectively (Sgro 1975). If the cloud is denser than  $n_{\text{crit}}$ , the shocked cloud gas cools rapidly (‘cold’ cloud) and, after having reached a temperature below  $\sim 10^4 \text{ K}$ , it produces line emission of lower ionization stages of the constituent elements. In the ‘hot’ cloud case, the cloud density is lower than  $n_{\text{crit}}$  and the temperature is still higher than  $\sim 10^6 \text{ K}$  when the transmitted shock reaches the end of the cloud. The cloud emits X-rays and optical lines of higher ionization stages. However, there will be no region that has cooled down to  $\sim 10^4 \text{ K}$ , therefore no H $\alpha$  emission will be detected.

To estimate the properties of a hypothetical uniform cloud in the Lobe region, we use the values obtained in § 4 from the Sedov analysis of the EPIC data, i.e.  $v_s = 720 \text{ km s}^{-1}$  under the assumption of full equilibration between electrons and ions behind the shock, and  $n_0 = 0.16 \text{ cm}^{-3}$ . The critical density  $n_{\text{crit}}$  as a function of the cloud size  $a$  (eq. (5)) is plotted in Figure 9 for three different values for the density contrast  $\chi = 10, 100, \infty$ . The region below the line corresponds to the ‘hot’ cloud case, whereas the region above is the ‘cold’ cloud case. Assuming an ambient density of  $n_0 = 0.16 \text{ cm}^{-3}$ , the initial cloud density  $n_{\text{cloud}} = 1.6, 16$  for  $\chi = 10, 100$ , respectively.  $n_{\text{cloud}}$  is also indicated in the diagram with thin horizontal lines. As can be seen in Figure 9, for  $\chi = 100$  we would have the ‘cold’ cloud case for all clouds with  $a > 0.1 \text{ pc}$ . However, the observed soft X-ray emission from the Lobe indicates a ‘hot’ cloud case. If we assume a cloud size  $a = 1 \text{ pc}$  and a density contrast  $\chi = 10$ , equation (5) yields a critical density of  $n_{\text{crit}} = 3.7 \text{ cm}^{-3}$ , while a cloud size of  $a = 0.5 \text{ pc}$  with  $\chi = 10$  results in  $n_{\text{crit}} = 4.6 \text{ cm}^{-3}$ . For a likely cloud size  $a \approx 1 \text{ pc}$ ,  $\chi = 10$  would result in a ‘hot’ cloud. Therefore, the Lobe emission is indicative of an

interaction between the shock wave of CTB 109 ( $v_s = 720 \text{ km s}^{-1}$ ,  $n_0 = 0.16 \text{ cm}^{-3}$ ) and an interstellar cloud with a density  $n_{\text{cloud}} \lesssim 5 \text{ cm}^{-3}$ .

## 6. Summary

We have studied the Galactic SNR CTB 109 using EPIC data of five *XMM-Newton* pointings. The deep EPIC image, created from all of these observations, shows no emission in the western part of the shell. This confirms that the remnant has its semi-circular morphology because the progress of the shock wave has been stopped by the GMC. We find no morphological evidence for a connection between the Lobe and the pulsar. The mosaic RGB image reveals some regions and clumps within the remnant which appear to have harder or softer spectra than the average spectrum. However, a detailed spectral analysis indicates that only two regions have significantly different fitted values for the  $N_{\text{H}}$ , temperature, or ionization timescale. The Lobe region appears to have rather small spectral variations.

Using the RGB composite image as a guide, we extract spectra for different parts of the remnant in circular regions as well as polygon regions. Best fit results are obtained with a single-temperature non-equilibrium ionization model for a collisional plasma. Abundances are determined for Mg and Si, while the abundances of the other elements are fixed to solar values. As the spectra show no indication of nonthermal emission, we derive upper limits in the energy range of 0.3 – 10.0 keV. In the eastern part of the shell where emission is believed to arise from the forward shock the upper limit of nonthermal emission is less than 2% of the thermal emission.

Analysis of the spectra of four regions in the Lobe indicates that the spectral variations seen in the RGB composite image are caused by small differences in temperature, ionization timescale of the plasma, as well as  $N_{\text{H}}$ . None of these differences are significant at the 90% confidence level. There is no significant evidence for nonthermal emission from the Lobe. The upper limits of the nonthermal emission are low; the flux upper limit for the entire Lobe in the energy range of 0.3 – 10.0 keV is  $6.9 \times 10^{-14} \text{ ergs cm}^{-2} \text{ s}^{-1}$  with an average surface brightness of  $1.1 \times 10^{-15} \text{ ergs cm}^{-2} \text{ s}^{-1} \text{ arcmin}^{-2}$ ,

about five times lower than the flux from the X-ray jet of the Vela pulsar. The detailed spectral analysis shows that the spectra of the Lobe and the remnant shell are remarkably similar, with  $kT = 0.50 - 0.70 \text{ keV}$ ,  $\tau = 1 - 3 \times 10^{11} \text{ s cm}^{-3}$ , and  $N_{\text{H}} = 5 - 7 \times 10^{21} \text{ cm}^{-2}$ . Mg and Si abundances turn out to be consistent with solar values in almost all analyzed regions of the SNR except in the bright central part of the Lobe where the Si abundance is slightly higher than solar ( $\sim 1.6 \pm 0.2$  times solar). This marginal indication of overabundance, only seen in one region of the SNR, is not indicative of ejecta emission. The small color variations seen in the RGB composite image do not result in significant differences in the fitted spectral parameters. We use the Mg line emission as an NEI line diagnostic. We fit the Mg XI triplet and Mg XII Ly $\alpha$  line features with Gaussians and derive a lower limit for  $kT$  which is consistent with the results from the global NEI fits of the EPIC spectra.

The detailed spectral analysis does confirm significant spectral variations for two locations within the remnant. The northeastern part of the shell, right next to a radio bright knot, contains a bright spot with lower temperature ( $kT \approx 0.3 \text{ keV}$ ) and higher ionization timescale ( $\tau = 4 - 6 \times 10^{11} \text{ s cm}^{-3}$ ). In this region, Fesen & Hurford (1995) have found two bright optical filaments. The high value for  $\tau$  indicates a region with a possibly higher density; it seems that the shock wave of the SNR has encountered a particularly dense cloud in this part of the shell. The region just north of the pulsar corresponding to the CO arm has a significantly higher  $N_{\text{H}}$  ( $\sim 1.0 \times 10^{22} \text{ cm}^{-2}$ ) than other regions in the remnant. The temperature and ionization timescale are mostly consistent with the rest of the remnant. We conclude that the underlying spectrum in this region is not significantly different from the spectrum of the rest of the remnant, but the column density of material in front of this part of the remnant is higher. We note that this larger value of  $N_{\text{H}}$  is consistent with what Woods et al. (2004) find for their fits to the spectrum of 1E2259+586 and hence strengthens the already-strong case for an association between the remnant and the pulsar. In addition, there is marginal evidence for a spectral variation with radius in the eastern shell of the SNR. The temperature is higher in the outer eastern shell, whereas

the  $N_{\text{H}}$  and  $\tau$  values are higher for the inner shell. This might indicate that the outer part of the shell (seen in projection) expands into a medium with lower density, while in the inner regions the shock is affected by density enhancements in the ISM.

From the result of the spectral analysis, we estimate an SNR blast wave velocity of  $v_s = 720 \pm 60 \text{ km s}^{-1}$  assuming that the remnant is in the Sedov phase and that there is full equilibration of the electron and ion temperatures right behind the shock front, and a remnant age of  $t = (8.8 \pm 0.9) \times 10^3 d_3 \text{ yr}$ , at an assumed distance of  $D = 3.0 d_3 \text{ kpc}$ . In the case of partial equilibration with  $T_e/T_s = 0.4$  as the lower limit, the blast wave velocity would be  $v_s = 1140 \pm 90 \text{ km s}^{-1}$  and the remnant age  $t = (5.6 \pm 0.6) \times 10^3 d_3 \text{ yr}$ . We also calculate a pre-shock density of the nuclei  $n_0 = (0.16 \pm 0.02) d_3^{-0.5} \text{ cm}^{-3}$ , initial energy  $E_0 = (7.4 \pm 2.9) \times 10^{50} d_3^{2.5} \text{ ergs}$  (full equilibration) or  $E_0 = (18.5 \pm 7.3) \times 10^{50} d_3^{2.5} \text{ ergs}$  ( $T_e/T_s = 0.4$ ), and swept-up mass of  $M = (97 \pm 23) d_3^{2.5} M_{\odot}$ .

The thermal nature of the X-ray emission of the Lobe as well as the optical filaments found at the southwestern edge of the Lobe are clear indications that the Lobe is the result of the SNR shock wave encountering an interstellar cloud ( $n_{\text{cloud}} \lesssim 5 \text{ cm}^{-3}$ ). We infer from derived shock velocities and densities that the shock wave traveled through the cloud on a timescale which was comparable to the cooling time of the shocked gas in the cloud. The cloud was heated to temperatures of  $\sim 10^6 \text{ K}$  and has not yet cooled down substantially, resulting in little optical emission.

We are grateful to V. Kaspi for providing the *XMM-Newton* data (Obs. ID 0038140101) of 1E2259+586. We would like to thank A. Read and M. Freyberg for useful discussion about the *XMM-Newton* EPIC background analysis. This work was supported by the NASA *XMM-Newton* grant NAG5-9914, NASA contracts NAS8-39073 and NAS8-03060, and in part by NASA grants GO0-1127X and GO1-2060X. This research has made use of the SIMBAD database, operated at CDS, Strasbourg, France.

## A. Calculating Non-equilibrium Line Emissivities

`neiline` calculates line emissivities (using the Raymond & Smith 1977 code in its 1993 update) for certain non-equilibrium conditions, specifically an ionizing or recombining plasma with astrophysical abundances. We used the code to calculate the line ratio diagnostics described herein, and feel it could be of general interest to the SNR community.

The code is quite simple. After reading in the input values, it initializes the Raymond & Smith (1977; 1993 update) plasma code, evolves the plasma, and outputs the requested emission. The user can set the abundances, the initial electron and ionization temperatures (the initial ionization temperature is used to set the initial ionization balance), the pressure, and the maximum time, ionization timescale, or minimum temperature for the model. The plasma evolution can be isothermal, isobaric, isochoric, or a special case where the plasma is isobaric until the temperature drops to a specified value after which it is isothermal. Except in the isothermal case, the electron temperature drops by a user-defined factor (default 2%), and the cooling, ionization balance evolution, and line emissivities are calculated by the Raymond & Smith code at each step in the evolution.

The code is written in C and Fortran, and is available at:  
<http://cxc.harvard.edu/cont-soft/software/NEIline.1.00.html> .

## REFERENCES

- Allen, G. E., Houck, J. C., & Sturmer, S. J. 2004, *Advances in Space Research*, 33, 440
- Allen, G. E., et al. 1997, *ApJ*, 487, L97
- Anders, E. & Grevesse, N. 1989, *Geochim. Cosmochim. Acta*, 53, 197
- Arendt, R. G. 1989, *ApJS*, 70, 181
- Aschenbach, B., et al. 2000, *Proc. SPIE*, 4012, 731
- Bamba, A., Yamazaki, R., Ueno, M., & Koyama, K. 2003, *ApJ*, 589, 827
- Bedogni, R. & Woodward, P. R. 1990, *A&A*, 231, 481
- Blair, W. P. & Kirshner, R. P. 1981, *Nature*, 291, 132
- Borkowski, K. J., Lyerly, W. J., & Reynolds, S. P. 2001, *ApJ*, 548, 820
- Borkowski, K. J., Sarazin, C. L., & Blondin, J. M. 1994, *ApJ*, 429, 710
- Brickhouse, N. S., Raymond, J. C., & Smith, B. W. 1993, *Bulletin of the American Astronomical Society*, 25, 864
- Chevalier, R. A. 1999, *ApJ*, 511, 798
- Coe, M. J., Davies, S. R., Fahlman, G. G., & Gregory, P. C. 1989, *MNRAS*, 238, 649
- Cox, D. P. & Anderson, P. R. 1982, *ApJ*, 253, 268
- Fahlman, G. G. & Gregory, P. C. 1981, *BAAS*, 13, 533
- Fahlman, G. G. & Gregory, P. C. 1983, in *IAU Symp. 101: Supernova Remnants and their X-ray Emission*, 445–453
- Fesen, R. A. & Hurford, A. P. 1995, *AJ*, 110, 747
- Gaensler, B. M., Arons, J., Kaspi, V. M., Pivovarovoff, M. J., Kawai, N., & Tamura, K. 2002, *ApJ*, 569, 878
- Gavriil, F. P., Kaspi, V. M., & Woods, P. M. 2003, *ApJ*, 607, 959
- Ghavamian, P., Rakowski, C. E., Hughes, J. P., & Williams, T. B. 2003, *ApJ*, 590, 833
- Gotthelf, E. V., Koralesky, B., Rudnick, L., Jones, T. W., Hwang, U., & Petre, R. 2001, *ApJ*, 552, L39
- Gregory, P. C. & Fahlman, G. G. 1980, *Nature*, 287, 805
- Gregory, P. C. & Fahlman, G. G. 1983, in *IAU Symp. 101: Supernova Remnants and their X-ray Emission*, 429–436
- Hamilton, A. J. S., Chevalier, R. A., & Sarazin, C. L. 1983, *ApJS*, 51, 115
- Heiles, C. 1964, *ApJ*, 140, 470
- Heydari-Malayeri, M., Kahane, C., & Lucas, R. 1981, *Nature*, 293, 549
- Hughes, V. A., Harten, R. H., Costain, C. H., Nelson, L. A., & Viner, M. R. 1984, *ApJ*, 283, 147
- Hughes, V. A., Harten, R. H., & van den Bergh, S. 1981, *ApJ*, 246, L127
- Hurford, A. P. & Fesen, R. A. 1995, *MNRAS*, 277, 549
- Israel, F. P. 1980, *AJ*, 85, 1612
- Itoh, H. 1978, *PASJ*, 30, 489
- . 1989, *PASJ*, 41, 853
- Iwasawa, K., Koyama, K., & Halpern, J. P. 1992, *PASJ*, 44, 9
- Jansen, F., et al. 2001, *A&A*, 365, L1
- Kaastra, J. S. 1992, *An X-Ray Spectral Code for Optically Thin Plasmas*, Internal SRON-Leiden Report, updated version 2.0
- Kaspi, V. M., Gavriil, F. P., Woods, P. M., Jensen, J. B., Roberts, M. S. E., & Chakrabarty, D. 2003, *ApJ*, 588, L93
- Kirsch, M. 2003, *EPIC status of calibration and data analysis*, XMM-SOC-CAL-TN-0018, issue 2.1
- Klein, R. I., Budil, K. S., Perry, T. S., & Bach, D. R. 2003, *ApJ*, 583, 245
- Klein, R. I., McKee, C. F., & Colella, P. 1994, *ApJ*, 420, 213

- Kompaneets, A. S. 1960, *Sov. Phys. Dokl.*, 5, 46
- Koralesky, B., Frail, D. A., Goss, W. M., Claussen, M. J., & Green, A. J. 1998, *AJ*, 116, 1323
- Kothes, R., Uyaniker, B., & Yar, A. 2002, *ApJ*, 576, 169
- Liedahl, D. A., Osterheld, A. L., & Goldstein, W. H. 1995, *ApJ*, 438, L115
- Lu, F. J., Wang, Q. D., Aschenbach, B., Durouchoux, P., & Song, L. M. 2002, *ApJ*, 568, L49
- Lumb, D. H. 2001, EPIC Background Files, XMM-SOC-CAL-TN-0016, issue 2.0
- Lumb, D. H., Warwick, R. S., Page, M., & De Luca, A. 2002, *A&A*, 389, 93
- Mac Low, M., McKee, C. F., Klein, R. I., Stone, J. M., & Norman, M. L. 1994, *ApJ*, 433, 757
- Mewe, R., Gronenschild, E. H. B. M., & van den Oord, G. H. J. 1985, *A&AS*, 62, 197
- Mewe, R., Lemen, J. R., & van den Oord, G. H. J. 1986, *A&AS*, 65, 511
- Monet, D. B. A., et al. 1998, *VizieR Online Data Catalog*, 1252
- Parmar, A. N., Oosterbroek, T., Favata, F., Pightling, S., Coe, M. J., Mereghetti, S., & Israel, G. L. 1998, *A&A*, 330, 175
- Patel, S. K., et al. 2001, *ApJ*, 563, L45
- Pavlov, G. G., Teter, M. A., Kargaltsev, O., & Sanwal, D. 2003, *ApJ*, 591, 1157
- Rakowski, C. E., Ghavamian, P., & Hughes, J. P. 2003, *ApJ*, 590, 846
- Raymond, J. C. & Smith, B. W. 1977, *ApJS*, 35, 419
- Read, A. M. & Ponman, T. J. 2003, *A&A*, 409, 395
- Rho, J. & Petre, R. 1997, *ApJ*, 484, 828
- Rho, J.-H. & Petre, R. 1993, *Bulletin of the American Astronomical Society*, 25, 1442
- Saken, J. M., Fesen, R. A., & Shull, J. M. 1992, *ApJS*, 81, 715
- Sedov, L. I. 1959, *Similarity and Dimensional Methods in Mechanics*, Academic Press, New York
- Sgro, A. G. 1975, *ApJ*, 197, 621
- Shull, J. M. 1980, *ApJ*, 237, 769
- Smith, R. K., Brickhouse, N. S., Liedahl, D. A., & Raymond, J. C. 2001, *ApJ*, 556, L91
- Sofue, Y., Takahara, F., & Hirabayashi, H. 1983, *PASJ*, 35, 447
- Strüder, L., et al. 2001, *A&A*, 365, L18
- Sun, M., Seward, F. D., Smith, R. K., & Slane, P. O. 2004, *ApJ*, 605, 742
- Tatematsu, K., Fukui, Y., Iwata, T., Seward, F. D., & Nakano, M. 1990, *ApJ*, 351, 157
- Tatematsu, K., Fukui, Y., Nakano, M., Kogure, T., Ogawa, H., & Kawabata, K. 1987, *A&A*, 184, 279
- Tatematsu, K., Nakano, M., Yoshida, S., Wiramihardja, S. D., & Kogure, T. 1985, *PASJ*, 37, 345
- Taylor, G. I. 1950, *Proc. R. Soc. London A*, 201, 159
- Tenorio-Tagle, G., Bodenheimer, P., & Yorke, H. W. 1985, *A&A*, 145, 70
- Turner, M. J. L., et al. 2001, *A&A*, 365, L27
- Vancura, O., Raymond, J. C., Dwek, E., Blair, W. P., Long, K. S., & Foster, S. 1994, *ApJ*, 431, 188
- von Neumann, J. 1947, *Los Alamos Sci. Lab. Tech. Series*, Vol. 7
- Wang, Z., Qu, Q., Luo, D., McCray, R., & Mac Low, M. 1992, *ApJ*, 388, 127
- Woods, P. M., et al. 2004, *ApJ*, 605, 378
- Xu, J. & Stone, J. M. 1995, *ApJ*, 454, 172

---

This 2-column preprint was prepared with the AAS L<sup>A</sup>T<sub>E</sub>X macros v5.2.

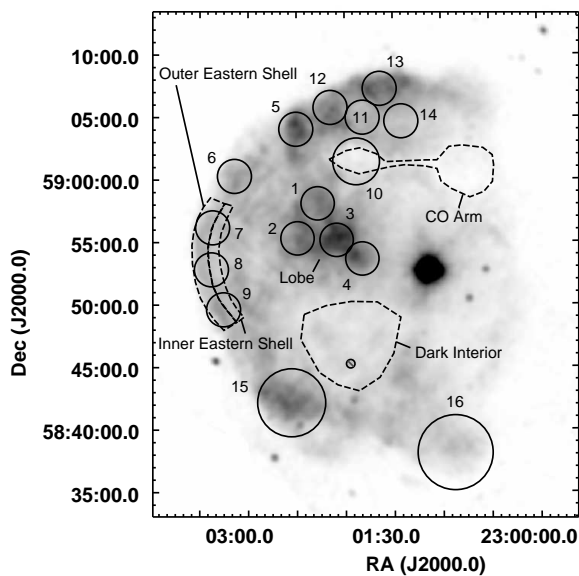


Fig. 3.— Mosaic of all five pointings towards CTB 109 in the energy band of 0.3 – 4.0 keV with analyzed regions. For circular regions, numbers as used in the paper are given, and the non-circular regions analyzed with `evigweight` are shown with dashed lines. A point source is excluded in the region ‘Dark Interior’ (small canceled circle).

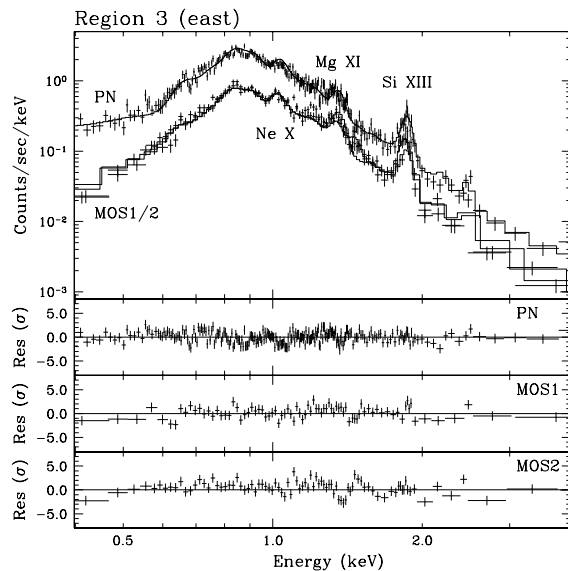


Fig. 5.— *XMM-Newton* EPIC spectra of the Lobe region 3 extracted from the pointing E data, with VNEI model fits. The position of the Ne X, Mg XI, and Si XIII lines is indicated. Instead of subtracting the background spectrum from the source spectrum, it has been modeled simultaneously. The displayed source spectrum and its fitted model include the background spectrum components. Background spectra are not plotted in this and the following spectrum figures.

Fig. 1.— See fig1.jpg.

Fig. 2.— See fig2.jpg.

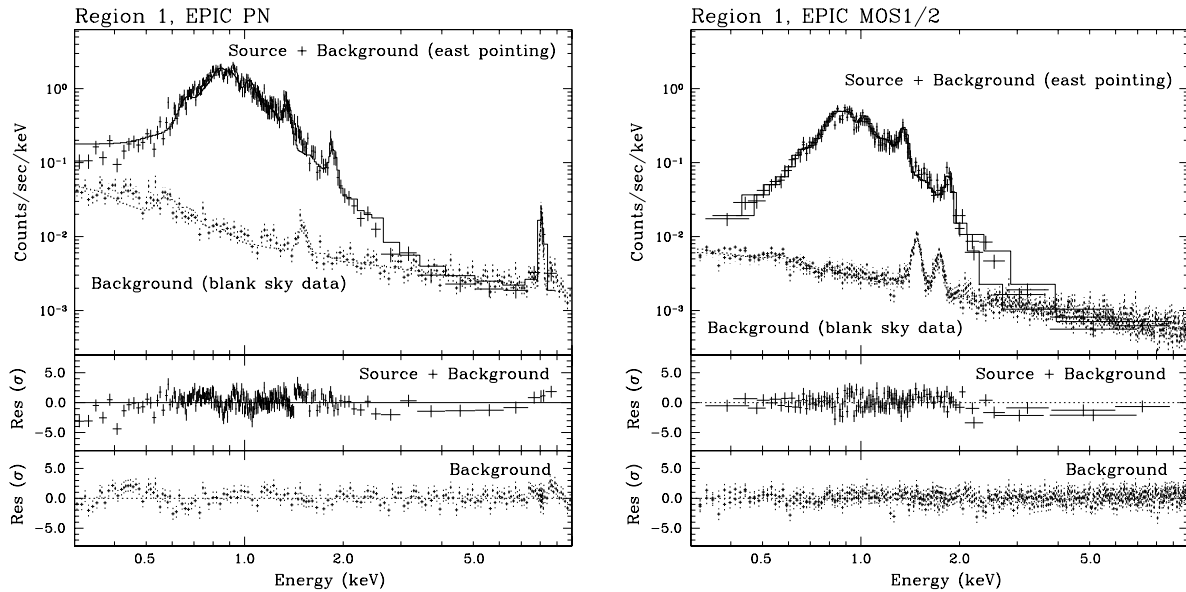


Fig. 4.— *XMM-Newton* EPIC spectra of the Lobe region 1 extracted from the pointing E data are shown with VNEI model fits for PN and MOS1/2. Solid line is used for source + background spectrum, dashed line for background spectrum. The background spectrum has not been subtracted from the source spectrum, but has been modeled simultaneously and is included in the spectral model of the source spectrum. Strong fluorescence lines are visible in the background spectra: Al-K line at 1.5 keV and Cu-Ni-Zn-K line complex around 8 keV in the PN spectrum (left), and Al-K at 1.5 keV and Si-K at 1.7 keV in the MOS spectra (right).

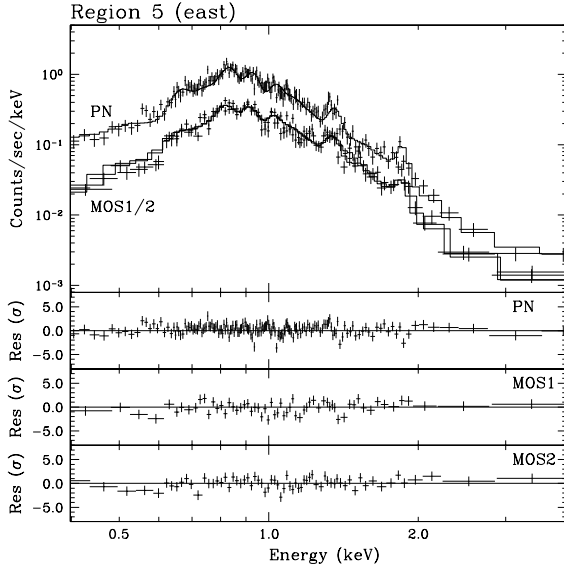


Fig. 6.— *XMM-Newton* EPIC spectra of the region 5 in the eastern part of the shell extracted from the pointing E data, with VNEI model fits. For background spectrum see the caption of Figure 5.

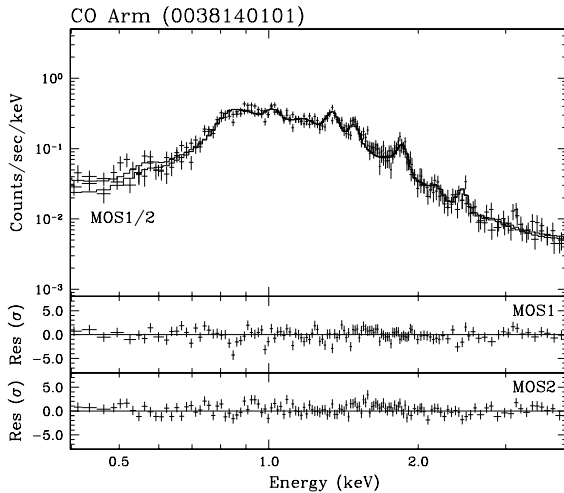


Fig. 7.— *XMM-Newton* EPIC MOS1/2 spectra of the CO arm (from pointing P1) with VNEI model fit. For background spectrum see the caption of Figure 5.

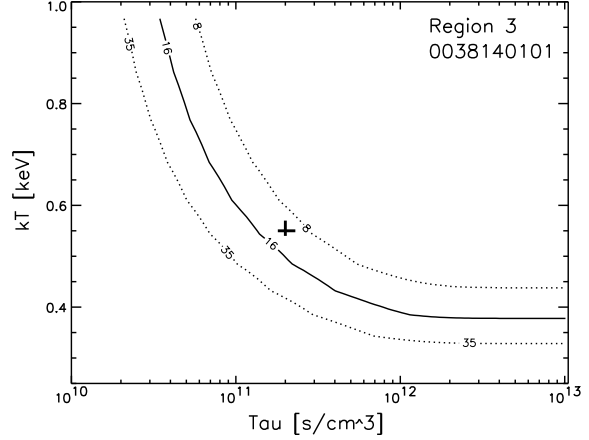


Fig. 8.— The line ratio Mg XI/Mg XII for region 3 derived from the spectral fits of P1 data is plotted as function of  $\tau$  and  $kT$  as solid line. The estimated range for the error is shown with dotted lines.  $kT$  and  $\tau$  values resulting from the global spectral analysis (0.3 – 10.0 keV with VNEI model) are plotted with 90% confidence errors.

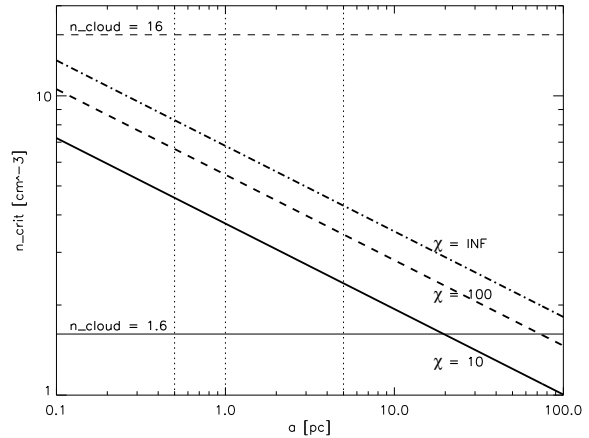


Fig. 9.— The critical density  $n_{\text{crit}}$  (Sgro 1975) as a function of cloud size  $a$  for  $v_s = 720 \text{ km s}^{-1}$  and  $n_0 = 0.16 \text{ cm}^{-3}$  (thick lines). Solid line is used for  $\chi = 10$ , dashed line for  $\chi = 100$ , and dash-dotted line for  $\chi = \infty$ . For  $\chi = 10, 100$ , the corresponding cloud density is shown with thin lines for  $n_0 = 0.16 \text{ cm}^{-3}$ . The dotted lines indicate  $a = 0.5, 1$  and  $5 \text{ pc}$ .

Table 1: *XMM-Newton* data used for the analysis.

Obs. ID <sup>a</sup>	Pointing direction		Inst. <sup>b</sup>	Mode <sup>c</sup>	Start time (UT)	Effective Exposure [ksec]
	RA	Dec				
	(J2000.0)					
00575401 (south, S)	23 01 25.2	58 41 45	PN	E. Full	2002-01-22 17:03:34	8.0
			M1	Full		11.0
			M2	Full		11.0
00575402 (north, N)	23 00 48.8	59 05 27	PN	E. Full	2002-07-09 07:58:03	6.0
			M1	Full		11.0
			M2	Full		11.0
00575403 (east, E)	23 02 23.1	58 53 30	PN	E. Full	2002-07-09 13:34:48	9.0
			M1	Full		11.0
			M2	Full		12.0
00381401 (P1)	23 00 57.6	58 53 43	M1	Full	2002-06-11 09:05:01	34.0
			M2	Full		34.0
01553503 (P2)	23 00 57.4	58 53 37	M2	Full	2002-06-21 09:35:31	17.0

<sup>a</sup>Throughout the paper, the observations are called S, N, E, P1, and P2, as indicated in the table.

<sup>b</sup>Instruments: PN: EPIC PN, M1: EPIC MOS1, M2: EPIC MOS2. All the analyzed data were obtained with the medium filter.

<sup>c</sup>Full: Full Window Mode, E. Full: Extended Full Window Mode.

Table 2: *XMM-Newton* spectral results of circular regions using the spectral model VNEI with solar abundances except for Mg and Si. Only results from the simultaneous fits of the MOS1 and MOS2 data are shown, whereas the paper discusses results from PN data as well. Blank sky data are used as background data.

Region	Pointing	$N_{\text{H}}(10^{22})$ [ $\text{cm}^{-2}$ ]	$kT$ [keV]	Mg (solar)	Si (solar)	$nt(10^{11})$ [ $\text{s cm}^{-3}$ ]	$\chi^2/\text{d.o.f}$
1	P1	$0.60^{+0.02}_{-0.10}$	$0.55^{+0.04}_{-0.03}$	$1.0^{+0.2}_{-0.1}$	$0.9^{+0.2}_{-0.1}$	$1.4^{+1.1}_{-0.1}$	896.1/702 = 1.3
2	P1	$0.51^{+0.05}_{-0.02}$	$0.59^{+0.02}_{-0.02}$	$0.9^{+0.1}_{-0.1}$	$1.2^{+0.2}_{-0.2}$	$2.0^{+0.1}_{-0.2}$	896.6/684 = 1.3
3	P1	$0.49^{+0.04}_{-0.03}$	$0.55^{+0.02}_{-0.01}$	$0.9^{+0.1}_{-0.1}$	$1.6^{+0.2}_{-0.2}$	$2.0^{+0.3}_{-0.2}$	904.3/721 = 1.3
4	P1	$0.49^{+0.04}_{-0.05}$	$0.53^{+0.03}_{-0.01}$	$0.9^{+0.1}_{-0.1}$	$1.2^{+0.2}_{-0.2}$	$2.8^{+1.0}_{-0.5}$	896.5/676 = 1.3
5	E	$0.82^{+0.07}_{-0.07}$	$0.29^{+0.03}_{-0.03}$	$0.7^{+0.2}_{-0.2}$	$1.9^{+0.9}_{-0.7}$	$4.0^{+4.1}_{-1.7}$	747.3/600 = 1.2
6	E	$0.51^{+0.07}_{-0.09}$	$0.64^{+0.09}_{-0.10}$	$1.3^{+0.4}_{-0.2}$	$1.0^{+0.3}_{-0.4}$	$1.0^{+0.6}_{-0.4}$	645.9/593 = 1.1
7	E	$0.68^{+0.11}_{-0.06}$	$0.63^{+0.10}_{-0.11}$	$1.1^{+0.3}_{-0.2}$	$1.0^{+0.4}_{-0.4}$	$0.8^{+0.6}_{-0.3}$	678.0/552 = 1.2
8	E	$0.67^{+0.03}_{-0.04}$	$0.62^{+0.04}_{-0.03}$	$1.0^{+0.3}_{-0.1}$	$0.8^{+0.2}_{-0.4}$	$0.7^{+0.2}_{-0.1}$	642.8/593 = 1.1
9	E	$0.54^{+0.49}_{-0.09}$	$0.57^{+0.11}_{-0.36}$	$1.0^{+0.6}_{-0.4}$	$1.2^{+0.8}_{-0.7}$	$1.4^{+1.4}_{-1.1}$	728.7/607 = 1.2
10	P1	$0.88^{+0.05}_{-0.02}$	$0.52^{+0.01}_{-0.02}$	$1.0^{+0.1}_{-0.2}$	$1.0^{+0.3}_{-0.1}$	$1.7^{+0.5}_{-0.3}$	1126.7/918 = 1.2
11	N	$0.79^{+0.22}_{-0.04}$	$0.53^{+0.05}_{-0.24}$	$0.8^{+0.1}_{-0.2}$	$0.6^{+0.2}_{-0.2}$	$0.9^{+0.5}_{-0.3}$	637.7/618 = 1.0
12	N	$0.70^{+0.26}_{-0.11}$	$0.48^{+0.13}_{-0.23}$	$1.0^{+0.1}_{-0.4}$	$1.0^{+0.3}_{-0.3}$	$1.1^{+2.8}_{-0.5}$	653.4/586 = 1.1
13	N	$0.67^{+0.33}_{-0.05}$	$0.52^{+0.05}_{-0.26}$	$1.0^{+0.1}_{-0.1}$	$0.9^{+0.3}_{-0.2}$	$1.4^{+0.3}_{-0.4}$	733.9/617 = 1.2
14	N	$0.93^{+0.14}_{-0.07}$	$0.42^{+0.05}_{-0.13}$	$0.8^{+0.3}_{-0.4}$	$0.8^{+1.7}_{-0.2}$	$1.8^{+N/A}_{-0.5}$	734.4/641 = 1.1
15	S	$0.54^{+0.01}_{-0.01}$	$0.60^{+0.02}_{-0.01}$	$1.0^{+0.1}_{-0.1}$	$1.0^{+0.2}_{-0.3}$	$0.8^{+0.1}_{-0.2}$	1549.8/1325 = 1.2
16	S	$0.57^{+0.01}_{-0.01}$	$0.60^{+0.03}_{-0.01}$	$1.1^{+0.1}_{-0.1}$	$0.9^{+0.3}_{-0.2}$	$1.0^{+0.1}_{-0.2}$	1646.6/1475 = 1.1

Table 3: *XMM-Newton* spectral results of arc-shaped region in the eastern part of the shell, the CO arm, and the low surface brightness region in the southern interior, using `evigweight`. The fit results are from the analysis of MOS1/2 data using the VNEI model; abundances are fixed to solar values except for Mg and Si. ‘Closed’ data are used as background data.

Region	Pointing	$N_{\text{H}}(10^{22})$ [ $\text{cm}^{-2}$ ]	$kT$ [keV]	Mg (solar)	Si (solar)	$nt(10^{11})$ [ $\text{s cm}^{-3}$ ]	$\chi^2/\text{d.o.f}$
Outer E. Shell	E	$0.59^{+0.02}_{-0.01}$	$0.68^{+0.02}_{-0.02}$	$1.1^{+0.2}_{-0.1}$	$0.9^{+0.2}_{-0.2}$	$0.7^{+0.1}_{-0.2}$	$566.7/405 = 1.4$
Inner E. Shell	E	$0.67^{+0.04}_{-0.06}$	$0.60^{+0.05}_{-0.04}$	$1.1^{+0.1}_{-0.2}$	$0.9^{+0.2}_{-0.2}$	$1.1^{+0.3}_{-0.3}$	$347.8/267 = 1.3$
CO Arm	P1	$0.97^{+0.02}_{-0.01}$	$0.54^{+0.01}_{-0.01}$	$0.9^{+0.1}_{-0.2}$	$0.9^{+0.2}_{-0.1}$	$1.5^{+0.4}_{-0.2}$	$918.5/732 = 1.3$
Dark Interior	P1	$0.66^{+0.03}_{-0.07}$	$0.53^{+0.05}_{-0.03}$	$1.0^{+0.1}_{-0.2}$	$0.9^{+0.1}_{-0.2}$	$1.5^{+0.4}_{-0.3}$	$1452.5/1074 = 1.4$

Table 4: Results of the Mg line analysis from *XMM-Newton* EPIC MOS data (pointings P1 and P2) of the Lobe. The spectral model is ‘APEC No Line’ plus Gaussians.

Region	Mg XI triplet		Mg XII Ly $\alpha$	Mg XI triplet/Mg XII Ly $\alpha$
	$E$ [keV]	Norm <sup>a</sup>	Norm <sup>a</sup>	Line Ratio
P1, MOS1/2				
1 (North)	$1.337^{+0.009}_{-0.002}$	$1.1^{+0.1}_{-0.5} \times 10^{-4}$	$2.0^{+0.4}_{-0.5} \times 10^{-5}$	$5.5^{+2.5}_{-3.0}$
2 (East)	$1.338^{+0.008}_{-0.003}$	$9.7^{+1.3}_{-2.0} \times 10^{-5}$	$0.1^{+0.7}_{-0.1} \times 10^{-5}$	$97^{+\infty}_{-87}$
3 (Center)	$1.337^{+0.004}_{-0.002}$	$1.2^{+0.1}_{-0.2} \times 10^{-4}$	$7.7^{+5.3}_{-4.0} \times 10^{-6}$	$16^{+19}_{-8}$
4 (Southwest)	$1.340^{+0.006}_{-0.010}$	$7.2^{+1.8}_{-2.0} \times 10^{-5}$	$0.1^{+1.4}_{-0.1} \times 10^{-5}$	$72^{+\infty}_{-69}$
P2, MOS2				
1 (North)	$1.335^{+0.011}_{-0.010}$	$9.4^{+2.6}_{-6.1} \times 10^{-5}$	$1.8^{+0.8}_{-1.7} \times 10^{-5}$	$5.2^{+114.8}_{-3.9}$
2 (East)	$1.343^{+0.013}_{-0.008}$	$1.2^{+0.2}_{-0.3} \times 10^{-4}$	$0.8^{+1.8}_{-0.8} \times 10^{-5}$	$15^{+\infty}_{-12}$
3 (Center)	$1.335^{+0.006}_{-0.005}$	$1.3^{+0.5}_{-0.2} \times 10^{-4}$	$1.1^{+0.7}_{-1.0} \times 10^{-5}$	$12^{+168}_{-7}$
4 (Southwest)	$1.340^{+0.011}_{-0.010}$	$8.2^{+1.8}_{-4.0} \times 10^{-5}$	$0.3^{+0.8}_{-0.3} \times 10^{-5}$	$27^{+\infty}_{-23}$

<sup>a</sup>Norm = total number of photons/cm<sup>2</sup>/s/extraction area in the line.

This figure "fig1.jpg" is available in "jpg" format from:

<http://arxiv.org/ps/astro-ph/0408290v2>

This figure "fig2.jpg" is available in "jpg" format from:

<http://arxiv.org/ps/astro-ph/0408290v2>